2005

# Steady and unsteady modeling of single PEM fuel cell.

Wenbo Huang
*University of Windsor*

# STEADY AND UNSTEADY MODELING

# OF SINGLE PEM FUEL CELL

By

Wenbo Huang

A Thesis
Submitted to the Faculty of Graduate Studies and Research
through the Department of Mechanical, Automotive and Materials Engineering
in Partial Fulfillment of the Requirements for
the Degree of Master of Applied Science
at the University of Windsor

Windsor, Ontario, Canada
2005

*Your file Votre référence*
*ISBN: 978-0-494-17104-2*
*Our file Notre référence*
*ISBN: 978-0-494-17104-2*

## ABSTRACT

Among the various types of fuel cells, the proton exchange membrane (PEM) fuel cell has been considered as a promising choice for automobile. Proper water and thermal management is essential for obtaining high performance from a PEM fuel cell. A steady and unsteady, water and thermal management model was developed to consider the effects of local pressure on the cell performance, pressure drop, open circuit voltage variation with stack temperature, water vapor effects on membrane conductivity. These considerations made the model physically more reasonable and more suitable for various operating conditions. Additionally, this model combined the along-flow-channel model and catalyst layer model, which represent a significant improvement to PEM fuel cell modeling. The model can predict the distributions of a series of important parameters along the flow channel and in the catalyst layer; thus the effects of various operating and design parameters on the fuel cell performance can be investigated easily by a numerical trial-and-error method. The transient performance of the fuel cell can be simulated with this model as well, which is crucial for the fuel cell system control. The modeling results agreed reasonably with the available experimental results from the literature. This model can be used as part of a PEM fuel cell stack or entire system modeling, and represents a very useful engineering tool for the analysis, design and optimization of PEM fuel cell.

To

My parents, my parents-in-law

My wife and my son

For

Their love, support and understanding

## ACKNOWLEDGEMENTS

I would like to express my appreciation to my advisors Dr. Bill Zhou and Dr. Andrzej Sobiesiak for their supervision, support, encouragement and guidance throughout my Master program.

Also, I would like to thank Dr. Randy Bowers, Dr. David Ting who gave so much useful advice on my graduation proposal and thesis. I was motivated by their encouragement and high academic standard. Special thanks also go to Dr. Andrzej Sobiesiak for providing invaluable support in our experiments, and I must say a thank you to Dr. Gary Rankin to be the chair of my defense.

I would like to thank my colleagues in our team: Xiaochen Yu, Yi Zong, and Peng Quan, for their helpful advices, enduring support and cooperation. I am proud of our research group.

This work was supported by the Auto21 Networks of Centers of Excellence Grant D07-DFC.

# TABLE OF CONTENTS

## LIST OF FIGURES

## LIST OF TABLES

## NOMENCLATURE

| | |
|---|---|
| $A_g$ | heat exchange area per unit length (cm) |
| $A_k$ | cross-section area of stream $k$ channel ($m^2$) |
| $A_s$ | catalyst surface area per unit mass of the catalyst ($m^2\ g^{-1}$) |
| $A_v$ | the specific reaction surface area ($m^{-1}$) |
| $a$ | water activity |
| $c_m$ | water concentration in the membrane (mole $cm^{-3}$) |
| $c_{w,k}$ | water concentration at $k$ interface of the membrane (mole $cm^{-3}$) |
| $C_{O_2}$ | concentration of oxygen (mole $cm^{-3}$) |
| $C_{O_2,ref}$ | reference concentration of oxygen (mole $cm^{-3}$) |
| $C_{p,i}$ | heat capacity of species $i$ ($J\ mol^{-1}\ ^oC^{-1}$) |
| $d$ | channel height (cm) |
| $D$ | hydraulic diameter (m) |
| $D^0$ | intradiffusion coefficient of water in the membrane ($cm^2\ s^{-1}$) |
| $D_{O_2}$ | bulk oxygen diffusion coefficient |
| $D_w$ | diffusion coefficient of water ($cm^2\ s^{-1}$) |
| $D_{O_2-H_2O}$ | diffusion coefficient of oxygen in liquid water |
| $D_{O_2-m}$ | diffusion coefficient of oxygen in membrane |
| $D_{O_2}^{eff}$ | effective diffusion coefficient |
| $EC$ | excess coefficient |

| | |
|---|---|
| $E_{cell}$ | fuel cell voltage (V) |
| $E_{oc}$ | reversible open circuit voltage (V) |
| $f$ | friction factor |
| $F$ | Faraday constant (Col equivalent$^{-1}$) |
| $h$ | channel width (cm) |
| $I$ | local current density (A cm$^{-2}$) |
| $I^0$ | exchange current density for oxygen reaction (A cm$^{-2}$) |
| $I_{avg}$ | average current density (A cm$^{-2}$) |
| $I_{0,ref}$ | reference exchange current density (A cm$^{-2}$) |
| $k_c$ | condensation rate constant (s$^{-1}$) |
| $k_m$ | bulk conductivities of the ionomer |
| $k_m^{eff}$ | effective conductivity of the ionomer in the catalyst layer |
| $k_p$ | hydraulic water permeability (cm$^2$) |
| $k_s$ | bulk conductivities of the solid catalyst |
| $k_s^{eff}$ | effective conductivity of the catalyzed solid in the catalyst layer |
| $l_m$ | the ratio of the volume occupied by the ionomer to the total void space available in the catalyst layer |
| $L$ | flow channel length (cm) |
| $m_{Pt}$ | catalyst mass loading per unit area of the cathode (mg cm$^{-2}$) |
| $M_i$ | molar flow rate of species $i$ (mole s$^{-1}$) |
| $n_d$ | electro-osmotic coefficient of water in membrane |
| $N_i$ | y-component molar flux of species $i$ (mole cm$^{-2}$ s$^{-1}$) |
| $P$ | local total pressure (atm) |

| | |
|---|---|
| $P_i$ | local partial pressure of species *i* (atm) |
| $Q$ | local flow rate ($m^3\ s^{-1}$) |
| $R$ | gas constant (82.06 $cm^3$ atm $mol^{-1}\ K^{-1}$) |
| $Re$ | Reynolds number |
| $R_u$ | universal ideal gas constant (8.3144 J $mol^{-1}\ K^{-1}$) |
| $t_m$ | membrane thickness (cm) |
| $T$ | local temperature (°C) |
| $T_{1\sim8}$ | the certain temperature used for interpolation of physical properties |
| $U$ | overall heat-transfer coefficient between channel and solid layer ($J\ s^{-1}\ cm^{-2}\ °C^{-1}$) |
| $V$ | local velocity ($m\ s^{-1}$) |
| $W_{m,dry}$ | equivalent weight of a dry membrane ($g\ mol^{-1}$) |

*Greek*

| | |
|---|---|
| $\alpha$ | net water flux per proton |
| $\alpha_a$ | anode transfer coefficient |
| $\alpha_{area}$ | effective area coefficient |
| $\alpha_c$ | cathode transfer coefficient |
| $\phi$ | relative water content |
| $\eta_{act}$ | voltage loss due to activation (V) |
| $\eta_{ohmic}$ | voltage loss due to ohmic resistance (V) |
| $\rho$ | local average density ($kg\ m^{-3}$) |

| | |
|---|---|
| $\rho_c$ | density of carbon black (g $cm^{-3}$) |
| $\rho_{m,dry}$ | density of dry membrane (g $cm^{-3}$) |
| $\rho_{Pt}$ | density of platinum (g $cm^{-3}$) |
| $\delta$ | catalyst layer thickness (μm) |
| $\phi_c$ | void fraction of catalyst layer |
| $\gamma$ | the reaction order is usually taken as unity |
| $\mu$ | local average viscosity (kg $m^{-1}$ $s^{-1}$) |
| $\mu_w$ | water viscosity (g $cm^{-1}$ $s^{-1}$) |
| $\sigma_m$ | membrane conductivity, S $cm^{-1}$ |
| $\Delta H_{vap}$ | enthalpy of water evaporation/condensation (J $mol^{-1}$) |

*Superscripts and subscripts*

| | |
|---|---|
| $a$ | anode |
| $c$ | cathode |
| $H_2$ | hydrogen |
| $O_2$ | oxygen |
| $N_2$ | nitrogen |
| $k$ | anode or cathode |
| $l$ | liquid |
| $v$ | vapor |
| $w$ | water |
| $sat$ | saturated |

# 1. INTRODUCTION

Environmental concerns and the increasing dependence on imported fuels call for alternative energy sources and better utilization of existing energy sources. Most current automobiles are driven by internal combustion engines, which consume fossil fuel and generate air pollution. With the increasing public concern for environment protection, it is predictable that more and more strict regulations will be enforced to reduce or limit the emission of these vehicles in the future. For example, California's zero emission vehicle (ZEV) mandate [1] requires 10% of the vehicles sold by the automotive manufacturers after year 2004 to be ZEVs [2]. Similarly, European auto companies are required to meet their voluntary carbon dioxide emission limits set by the European Union [3]. According to Kyoto Protocol, international community is committed to cut greenhouse gases emission step by step. The Carbon Dioxide ($CO_2$) emitted by automobile is one of the most important parts of greenhouse gases. Governments like Canada have already invested a lot in exploring new ways to replace the internal combustion engine in automobiles. Among all the technical proposals, fuel cell is one of the most potential and feasible solutions to achieve this goal. The benefits of using fuel cells are following [4]: Firstly, fuel cells consume hydrogen instead of the exhaustible fossil fuel, which eventually protect our natural resource and environment; secondly, fuel cells emit only water, therefore, there is no pollution at all. Among all the currently existing fuel cell, proton exchange membrane (PEM) fuel cells has been widely considered as one of the most promising candidates for automobiles since it has one additional advantage over many other fuel cells. In this thesis, our research will focus on the PEM fuel cell related

topics. [5]

PEM fuel cells are efficient and clean power sources, which are being developed for both stationary and mobile applications. The polymer electrodes work at low temperature, which brings the further advantage of quick start-up for a PEM fuel cell. The thin dimensions of MEAs means that compact fuel cells could be made. Further advantages are that there are no corrosive fluid hazards, and that the cell could work in any orientation. This means that the PEM fuel cell is particularly suitable for use in vehicles and portable applications. During last decade, with increasing environmental concerns over vehicle-generated pollutions and limited range associated with battery-powered electric vehicles, the PEM fuel cell system has been gaining more attention as an alternative power generation device. Attractive characteristics of PEM fuel cells include its simple design and operation, $CO_2$ tolerance, better driving range and refuelling time, comparing with conventionally power devices such as batteries and internal combustion engines [6].

But currently most PEM fuel cells can only operate at low current densities in order to have a high efficiency [7]. When high power density performance is obtained, it is achieved at the sacrifice of energy efficiency. Recent work has shown that water and thermal management is one of the keys for achieving high power density performance as well as high efficiency.

Before we continue the discussion of our research topics, it is necessary to review a little about the progresses of fuel cell research and development. The fuel cell idea has been known for over 150 years. Although the first fuel cell was built by Sir William Grove in 1839, it was until the 1960s that the PEM fuel cell was invented at General

Electric in U.S. This PEM fuel cell was used by NASA on their first manned space vehicle. Since early 1980s, the British Royal Navy began to adopt this technology in their submarine. Since then, many companies and institutes around the world actively work on fuel cells to improve its safety, performance and low its costs. In 1995, a Vancouver company named Ballard Power, tested the PEM cell on the buses of Vancouver and Chicago, and later DaimlerChrysler put the PEM fuel cells in their experimental vehicles as well.

Although the PEM fuel cell technology has been successfully demonstrated, the performance of fuel cell still needs to be improved before they can be used as viable commercial products. One of the technical issues in fuel cell development is water and thermal management. On the one hand, fuel cells, just like any other energy conversion device, are not 100% efficient [8]. Part of fuel energy cannot be converted to useful electrical energy and has to be rejected as waste heat to ambient by the convection. Hence, heat rejection becomes important consideration in fuel cell design. Furthermore, PEM fuel cells need water to humidify the air and fuel. They also produce water during the reactions. It is necessary remove the excessive produced water and achieve "water balance" inside the PEM fuel cell. Since previous researches showed that water and heat management have great influence on the fuel cell's performance, a further study about the flow behavior inside the PEM module can be very meaningful [5].

In the present study, a steady and unsteady mathematical model with mass and energy balance in a single PEM fuel cell was developed to provide an understanding of the flow characteristics in the flow channels and catalyst layer. The transient performance

of the fuel cell can be simulated with this model as well. The model represents a useful engineering tool for the design and optimization of PEM fuel cell.

# 2. PRINCIPLES OF PEM FUEL CELL

This chapter describes the basic working principle of the PEM fuel cell, how the PEM fuel cell stack works and what the major concerns are in fuel cell system set up.

## 2.1 PEM Fuel Cell Working Principle

A typical sandwich construction of a single PEM fuel cell is shown in Fig. 1. It consists of a proton-exchange membrane, two active layers and electrodes, and two plates with channels at cathode and anode.

The proton-exchange membrane is a very thin polymer membrane which lies in the middle of a single cell and between the two active layers and electrodes. The most well-known polymer material is called Nafion made from fluoroethylene and manufactured by Dupont. Other kinds of membrane are also available, such as those made from new perflourosulfonic acids. Many fuel cell companies claim that they developed their own membrane which is more efficient and durable. Commonly, the thickness of membrane is between 0.0508 mm to 0.1778 mm [4]. Thin membranes generally have better performance, lower mechanical stability and lower overall life times [5].

The proton-exchange membrane plays an important role in a PEM fuel cell since it has a set of very special characteristics. One of its characteristics is that only hydrogen ions and water molecules can migrate through the proton-exchange membrane. The hydrogen gas, oxygen gas and electrons, on the other hand, cannot pass through it. Therefore, even though the proton-exchange membrane separates reactants, it will allow

the electrochemical reaction happen. Another property of proton-exchange membrane is that the proton conductivity is directly proportional to the water content. The higher the water content is, the more the water molecules can pass through the membrane and the better performance can be obtained. However, sometimes there is too much water to be fully taken away by the reactant. The water will block the pores in the electrodes and slow down the reaction speed, which leads to the downgrade of the fuel cell performance. Therefore, the water management in the proton-exchange fuel cell is considered as a significant factor which affects the fuel cell performance [5].

The active layer and electrode is a thin layer of porous carbon cloth or carbon paper that contains a light platinum coating on one face of each electrode. In the early days of PEM fuel cell development, platinum coating was used at the rate of 28 mg $cm^{-2}$. This is a major factor in the cost of a PEM fuel cell. Recently, the usage of platinum has been reduced to around 0.2 mg $cm^{-2}$ [9], which cuts the price of PEM fuel cell greatly. Usually, a fuel active layer and electrodes, a membrane and an oxidant active layer and electrodes are assembled as a very thin item, which is called membrane electrode assembly (MEA).

The outer parts of a single PEM are plates which usually made from stainless steel or carbon graphite, containing many tiny channels. Those plates have the following functions: 1. deliver hydrogen and oxygen to the MEA; 2. remove the water and waste heat that are generated in the fuel cell reaction; 3. collect the current produced by MEA. The reactants (hydrogen and oxygen) flow along the channels at the anode plates and cathode plates respectively. When the hydrogen gas flows along the channels, it diffuses into the active layer and contact with platinum catalysts, hydrogen releases electrons and creates hydrogen ions. The electrochemical reaction on the anode side is

[4]: $2H_2 \rightarrow 4H^+ + 4e^-$. On the cathode side active layer, an electrochemical reaction takes place when oxygen combines with hydrogen ions, which migrated through the membrane, and the electrons. Water is produced and heat is released. The chemical reaction that occurs on the cathode side is: $O_2 + 4e^- + 4H^+ \rightarrow 2H_2O + q_{rxn}$ [5].

Overall view of this device, when we continue feed hydrogen and air, there will have a stable electrical current from anode to cathode via the external circuit. Water appears in the cathode channel, and reaction heat will increase the temperature of both streams and solid.

$$\begin{aligned} &\textit{Anode}: \quad H_2 \Leftrightarrow 2H^+ + 2e^- \\ &\qquad\qquad\quad \downarrow \quad \downarrow \\ &\textit{Cathode}: \quad 2H^+ + 2e^- + 1/2O_2 \Leftrightarrow H_2O \\ &\textit{Overall}: \; H_2 \qquad\quad + 1/2O_2 \Leftrightarrow H_2O \end{aligned}$$

The potentials formed by anode hydrogen ions and cathode electrons will output as the cell voltage, and in general this voltage is around 0.6~0.7 volts for per cell. Because each single cell's output power is limited, a bank of cells will be assembled serially in real application in order to achieve higher power output and current collector will make a conducting bridge between the cells. Depend on the number of cells, and the active area of each cell, the total stack power can be in the range of several watts to hundreds kilowatts. PEM fuel cells have excellent start up and turndown abilities, it is a quiet device due to the fact there are no moving parts. They have zero emissions which makes it an environmentally friendly source of energy. Finally solid electrolytes make it corrosion and leakage free. All these advantages make PEM fuel cells a promising

technology in transportation industry [10].

## 2.2 PEM Fuel Cell Stack and System

For all applications of PEM fuel cells, whatever an on board engine, stationary power plant or in a CHP system, there are at least the following basic components in the system: the fuel cell stack which consists of a series of single fuel cells, the fuel supply system, the air supply system, the cooling and humidification system.

The fuel cell stack is key component inside which the electrochemical reactions happen. It generates the electricity and provides power to external circuit. The cooling system is another important component of fuel cell system. Since there will be thermal energy produced as the byproduct, a cooling system is need to removed the waste heat. The fuel supply system, possibly from a high pressure container or a hydrogen-produced reformer. PEM fuel cells must use pure hydrogen gas as the fuel, which is obtained from some fossil fuels such as petroleum or natural gas to coal or bio-fuels such as methanol and ethanol. Before these raw primary fuels are supplied to the stack, fuel reforming and processing is the essential method to guarantee that the feeding gas meet the particular stack fuel requirement. The most common reforming methods include stream reforming, partial oxidation reforming (POX), catalyst partial oxidation reforming (CPOX) and auto thermal reforming (ATR). The air is introduced into the stack at certain pressure by a pump or blower. High inlet pressure will increase the oxygen partial pressure on the catalyst layer, and will speed up the chemical reaction which achieves higher cell output voltage. However it will also cause lower system efficiency by consuming more electrical

power. Generally the fuel cell unit will operate at 70~90°C for optimal performance. To improve the efficiencies of fuel cell unit, both the hydrogen and oxidant supply need be humidified before they enter the fuel cell stack. [5] [10]

# 3. LITERATURE REVIEW AND OBJECTIVES

## 3.1 Literature Review

Costamagna *et al.* [11] gave a very good review about the fuel cell science and technology up to the year 2000. Another recent review made by Yao *et al.* [12] presents both empirical performance models and theoretical models.

To study the transport of water and ions in a PEM fuel cell, many researches have developed models at various levels of complexity. One-dimensional PEM fuel cell models were developed in the early 1990s. Verbrugge and Hill [13] [14] developed various half-cell and full-cell models. Bernardi and Verbrugge [15] [16] developed various models to study the effects of the transport of gases and water vapour in gas-diffusion electrodes on the performance of PEM fuel cells. In these models, the membrane was assumed to be uniformly hydrated with constant transport properties. The model of Springer *et al.* [17] [18] accounted for the dependence of the electro-osmotic coefficient on the water content within the membrane, gas transport within the diffusion layer of the electrodes, and water transport across the membrane by electro-osmotic force and back diffusion. All these models were isothermal and unsuitable for water and thermal management studies.

Nguyen and White [7] and Fuller and Newman [19] developed two-dimensional heat and water transport models that accounted for variations in the gas phase compositions, temperature and membrane hydration condition along the channels. An improved two-dimensional model was presented by Yi and Nguyen [20]. In this model,

cell performance with different design schemes was compared. Marr and Li [21] presented a simplified model for engineering applications and yet incorporated most fundamental physical and electrochemical processes. Ge and Yi [22] presented a two-dimensional, steady state model to describe the effect of flow mode (coflow and counterflow) and operating conditions on the performance of a PEM fuel cell.

In all these models, however, the pressure effect and pressure drop in the channels were neglected. In fact, the pressure loss in the fuel cell flow channel is one of the important factors that must be addressed for system optimal design, especially when using air instead of pure oxygen in serpentine channels. Based on the currently available publications on fuel cell modeling, there is little information regarding pressure effects on fuel cell performance.

To obtain the optimal performance, it is necessary to optimize the pressure drops in the flow channel. A higher pump power is needed to overcome higher pressure drop, which would reduce the overall efficiency of the system. On the other hand, a large pressure drop can be beneficial for water management. In addition, different local gas total pressure leads to different local partial pressure of reactant, water vapor and water activity, which is related to membrane performance.

Maharudrayya *et al.* [23] presented a CFD-based simulation regarding pressure losses in channels. But the physical and electrochemical processes in PEM fuel cells were not considered in their research.

Marr and Li [24] developed the performance modeling of catalyst layer in a proton exchange membrane fuel cell in the direction across the MEA, in which the composition and performance optimization of cathode catalyst platinum and catalyst layer structure

has been investigated by including both electrochemical reaction and mass transport process. The model was based on that the performance parameters along flow channel direction are uniform, which is not reasonable in practice.

For recent modeling studies, there are two categories; one is the along - channel modeling, which assumed that the MEA is ultra-thin and made simplification on corresponding calculation, the other one is based on the direction perpendicular to the MEA and assumed the uniform performance along flow channel. Both of them have some certain limitations which can not reflect the real case.

Another issue should be noticed is that among all the available literature, only the anode water activity was used for the calculation of membrane performance, which would lead to unreasonable high ohmic losses.

According to these understandings, in the present study, a steady and unsteady, water and thermal management model was proposed to consider pressure effects, pressure drop calculation, effects of both anode and cathode water vapor on membrane conductivity. And the effects of various operating and design parameters on the performance of PEM fuel cell were investigated. This model incorporates most of the essential fundamental physical and electrochemical processes occurring in the membrane, electrolyte, cathode catalyst layer, electrode backing and flow channel.

### 3.2 Objectives

Fuel cell designers either want to predict the system performance after the inlet condition is employed, or they want to optimize their design pattern to achieve highest

system efficiency by changing inlet parameters. Instead of a serial experimental test, a powerful calculation/simulation tool is required to determine PEM fuel cell power and thermal performance. The designation period between system modeling and concept design will thus be greatly shortened.

The purpose is to develop a fuel cell simulation/calculation tool based on fluid mechanics, heat transfer, thermodynamics and the electrochemical model. Using such a simulation tool, the fuel cell designer can compare different designs scheme efficiently. In order to enhance the precision and generality of the model, improvements have been implemented by considering:

1. Steady and unsteady state.
2. Local pressure on the cell performance.
3. Pressure drop along flow channel.
4. Open circuit voltage variation with stack temperature.
5. Water vapor effects on membrane conductivity.
6. Composition and performance of cathode catalyst platinum and catalyst layer structure.

This improved model allows a wide range of fuel cell simulations, which more accurately reflect the actual case. The model is a very useful engineering tool for the design and optimization of PEM fuel cells.

# 4. MATHEMATICAL MODEL

In this chapter, the model will be introduced which includes the following parts:

- Mass balance
- Energy balance
- Pressure loss
- Cell potential and current density
- Catalyst layer model

Fig. 1 shows the typical schematic diagram of a single PEM fuel cell with the flow channel in $x$-direction, and the $y$-direction is normal to the membrane. Fig. 2 shows the layout of a serpentine channel for simulation.

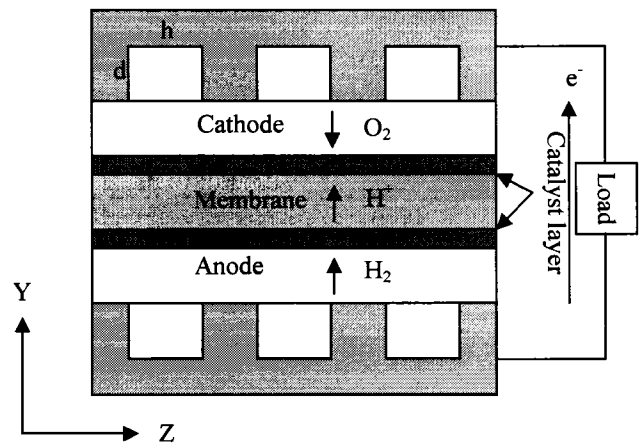


Fig. 1. Schematic diagram of PEM fuel cell

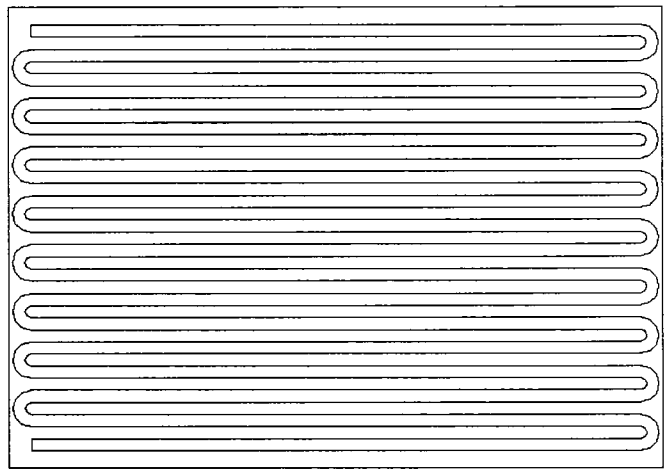

Fig. 2. Layout of a serpentine channel

### 4.1 Assumptions

For modeling purposes, the following assumptions were made in the present study:

1. Ideal gas law was employed for gaseous species.
2. Water transport in and out of the electrodes was in the form of vapour.
3. The gas transport resistance through the electrode porous layer could be neglected, i.e., the electrodes were assumed to be "ultra-thin".
4. The liquid water was assumed to exist at the surface of the channels, and the volume to be negligible.
5. For the pressure drop calculation, the entrance and exit effects were neglected, which were too small compared with the overall pressure drop.
6. No potential drop along the channels was assumed.

## 4.2 Mass Balance

The variation of gas flow rate along the channels was due to the flux $N_i(x)$ in the y-direction or products into or out of the membrane electrode assembly, which could be described as following modified equation based on that by Nguyen [7].

$$\frac{dM_i(x)}{dx} = -h_k \cdot \alpha_{area,k} \cdot N_i(x) \tag{1}$$

where $i$ is $H_2$, $O_2$ or $N_2$, and $\alpha_{area,k}$ is the effective area coefficient which reflects actual active area because of diffusion of reactants. The flux $N_i(x)$ is the function of coordinate $x$ because the current density varies along this direction. The molar fluxes of the anode and cathode components are described by:

$$N_{H_2}(x) = \frac{I(x)}{2F} \tag{2}$$

$$N_{O_2}(x) = \frac{I(x)}{4F} \tag{3}$$

$$N_{N_2}(x) = 0 \tag{4}$$

where $I(x)$ is local current density which varies along the channel due to the variation of water content, activation loss, ohmic loss, membrane conductivity and temperature.

The variation of water molar flow rate is due to y-component flux, electrochemical reaction products, evaporation and condensation as described here [7]:

Liquid water

$$\frac{dM_{w,k}^{l}(x)}{dx} = \left\{\frac{k_c h_k d_k}{R[T_k(x)+273]}\right\}\left\{\frac{M_{w,k}^{v}(x)}{M_{w,k}^{v}(x)+M_{gas}(x)}P_k(x) - P_{w,k}^{sat}(x)\right\} \tag{5}$$

Water vapor

$$\frac{dM_{w,k}^{v}(x)}{dx} = -\frac{dM_{w,k}^{l}(x)}{dx} - h_k \cdot \alpha_{area,k} \cdot N_{H_2O,k}^{v}(x) \tag{6}$$

where $k_c$ is the homogeneous rate constant for the condensation and evaporation of water reaction, and subscript $k$ represents anode or cathode. $P_k(x)$ is the local pressure considering the pressure drop along the channel.

$$N_{H_2O,a}^{v}(x) = \frac{\alpha I(x)}{F} \tag{7}$$

$$N_{H_2O,c}^{v}(x) = -\frac{(1+2\alpha)I(x)}{2F} \tag{8}$$

where $\alpha$ represents the net water molecule flux per proton. There are three water transport mechanisms in the membrane [20], which can be seen from the Fig. 3: (i) electro-osmotic drag, which is caused by proton transport from the anode side to the cathode side of the membrane, (ii) back-diffusion by the concentration gradient of water

between the anode side and the cathode side, and (iii) convection by water vapour pressure gradient between the anode side and cathode side.

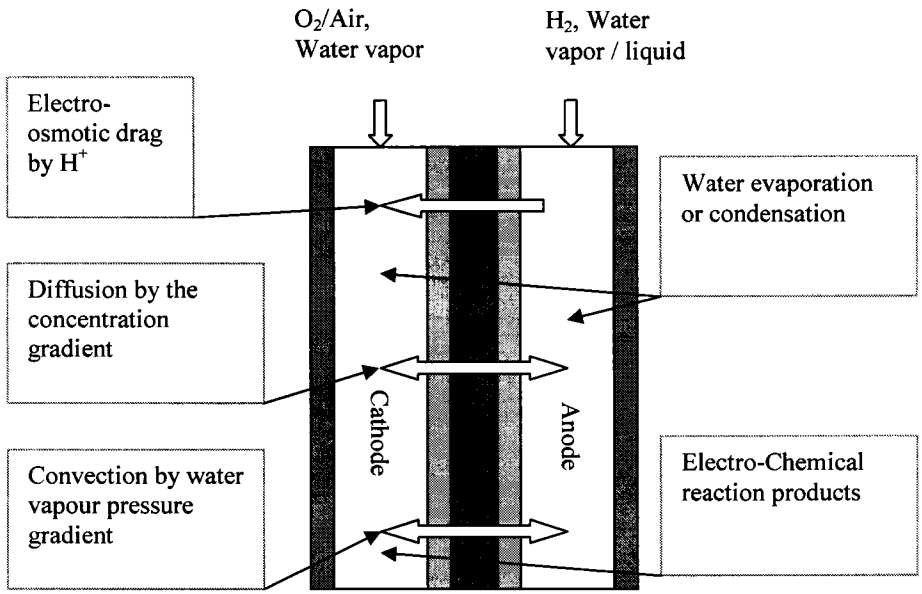


Fig. 3. Water transport mechanisms and balance

Therefore, $\alpha$ can be evaluated by the following equation [20]:

$$\begin{aligned}\alpha(x) &= n_d(x) - D_w(x)\frac{F}{I(x)}\frac{dc_w}{dy} - c_w\frac{k_p}{\mu}\frac{F}{I(x)}\frac{dP_w(x)}{dy} \\ &\approx n_d(x) - D_w(x)\frac{F}{I(x)}\frac{\{c_{w,c}(x) - c_{w,a}(x)\}}{t_m} \\ &\quad - \frac{\{c_{w,c}(x) + c_{w,a}(x)\}}{2}\frac{k_p}{\mu_w}\frac{F}{I(x)}\frac{\{P_{w,c}(x) - P_{w,a}(x)\}}{t_m}\end{aligned} \tag{9}$$

where $n_d$, $D_w$, $k_p$, $\mu_w$ and $t_m$ are electro-osmotic drag coefficient, diffusion coefficient of water, permeability of water in the membrane, water viscosity and membrane thickness respectively. The expressions given by Springer *et al.* [18] are used to calculate these parameters as listed below:

$$n_d = 0.0049 + 2.024a_a - 4.53a_a^2 + 4.09a_a^3 \qquad (a_a \le 1) \tag{10}$$

$$n_d = 1.59 + 0.159(a_a - 1) \qquad (a_a > 1) \tag{11}$$

$$D_w = D^0 \cdot n_d(x) \cdot \exp\left[2416\left(\frac{1}{303} - \frac{1}{273 + T_s}\right)\right] \tag{12}$$

The expressions for $c_{w,a}$, $c_{w,c}$, $P_{w,a}$, $P_{w,c}$ are given as follows.

$$c_{w,k} = \frac{\rho_{m,dry}}{W_{m,dry}}\left(0.043 + 17.8a_k - 39.85a_k^2 + 36.0a_k^3\right) \qquad (a_k \le 1) \tag{13}$$

$$c_{w,k} = \frac{\rho_{m,dry}}{W_{m,dry}}\left(14 + 1.4(a_k - 1)\right) \qquad (a_k > 1) \tag{14}$$

$$P_{w,a}(x) = \left(\frac{M_{w,a}^v(x)}{M_{w,a}^v(x) + M_{H_2}(x)}\right)P_a(x) \tag{15}$$

$$P_{w,c}(x) = \left(\frac{M_{w,c}^v(x)}{M_{w,c}^v(x) + M_{O_2}(x) + M_{N_2}(x)}\right)P_c(x) \tag{16}$$

where $\rho_{m,dry}$ and $W_{m,dry}$ are the density and equivalent weight of a dry proton exchange membrane. The water activities in the anode and cathode side are defined as

follows. $P_a(x)$ and $P_c(x)$ are the local pressures at anode and cathode respectively considering the pressure drop.

$$a_a = \left( \frac{M^v_{w,a}(x)}{M^v_{w,a}(x) + M_{H_2}(x)} \right) \frac{P_a(x)}{P^{sat}_{w,a}(x)} \tag{17}$$

$$a_c = \left( \frac{M^v_{w,c}(x)}{M^v_{w,c}(x) + M_{O_2}(x) + M_{N_2}(x)} \right) \frac{P_c(x)}{P^{sat}_{w,c}(x)} \tag{18}$$

The formulation for saturation pressure is expressed by [18].

$$\begin{aligned} \log_{10}(P^{sat}_w(x)) = {} & 2.95\times10^{-2} T_k(x) - 9.18\times10^{-5} T_k^2(x) \\ & + 1.44\times10^{-7} T_k^3(x) - 2.18 \end{aligned} \tag{19}$$

**4.3 Energy Balance**

The local temperatures in anode and cathode channels are affected by latent heat and heat transfer between the solid surface and the gas [7].

$$\frac{dT_k(x)}{dx} = \frac{UA_g(T_s(x) - T_k(x))}{\sum_i C_{p,i} M_i(x)} \tag{20}$$

The heart of the model is a spatial, time-dependent partial differential equation describing the local temperature of the solid cell support.

$$\rho_s C_s A_s \frac{\partial T_s(x)}{\partial t} = A_s k \frac{\partial^2 T_s(x)}{\partial x^2} + n_c A_g U_g \left[T_a(x) + T_c(x) - 2T_s(x)\right] + A_b U_b \left[T_{\inf} - T_s(x)\right] + n_c \left[H^v_{w,a} - H^l_{w,a}\right](x) \frac{dM^l_{w,a}(x)}{dx} + n_c \left[H^v_{w,c} - H^l_{w,c}\right](x) \frac{dM^l_{w,c}(x)}{dx} - e\left(\frac{\Delta H}{2F} + V_{cell}\right) I(x) \quad (21)$$

with boundary conditions

$$k \frac{\partial T_s(x)}{\partial x}\bigg|_{x=0} = U_c \left(T_s(x) - T_{\inf}\right)$$
$$k \frac{\partial T_s(x)}{\partial x}\bigg|_{x=L} = -U_c \left(T_s(x) - T_{\inf}\right) \quad (22)$$

The latent heat of evaporation or condensation can be calculated with the following equation [25].

$$\Delta H_{vap,k} = 45070 - 41.9 T_k(x) + 3.44 \cdot 10^{-3} T_k(x)^2 + 2.54 \cdot 10^{-6} T_k(x)^3 - 8.98 \cdot 10^{-10} T_k(x)^4 \quad (23)$$

### 4.4 Pressure Loss

In PEM fuel cell, the gas flow is usually in laminar regime because the channel size and gas flow rates are small. The pressure drop in a laminar flow strongly depends on the Reynolds number. The entrance and exit losses were neglected, which were too small

compared with the overall pressure drop if the channel is long enough. The flow was assumed fully developed.

Different local gas pressure leads to different partial pressure of reactant, water vapor and water activity, which is related to membrane performance. The expression of pressure loss in straight channel could be defined as Equation (24) [26], while that in curve channel could be defined as Equation (25).

$$\frac{dP_k(x)}{dx} = \rho_k(x) \cdot \left(\frac{1}{D_k}\right) \cdot \frac{V_k^2(x)}{2} \cdot f_k(x) \tag{24}$$

$$\frac{dP_k(x)}{dx} = \rho_k(x) \cdot \left(\frac{1}{D_k}\right) \cdot \frac{V_k^2(x)}{2} \cdot \left(f_k(x) + \frac{K_L \cdot D_k}{L_{curve}}\right) \tag{25}$$

where $P_k(x)$ is the local total gas pressure in the flow channel, $K_L$ is minor loss coefficient, the hydraulic diameter $D_k$ and the friction factor $f_k(x)$ are defined as below.

$$D_k = \frac{4h_k d_k}{2(h_k + d_k)} \tag{26}$$

$$f_k(x) = \frac{98}{\mathrm{Re}_x(x)} \tag{27}$$

$$\mathrm{Re}_k(x) = \frac{\rho_k(x) \cdot V_k(x) \cdot D_k}{\mu_k(x)} \tag{28}$$

where the $V_k(x)$ is local velocity, which is defined as below.

$$V_k(x) = \frac{Q_k(x)}{A_k} \tag{29}$$

The local average density $\rho_k(x)$ and average dynamic viscosity $\mu_k(x)$ can be calculated as follows [27]:

Anode:

$$\rho_a(x) = \left( \frac{M_{H_2}(x)}{M_{H_2}(x) + M^v_{w,a}(x)} \cdot \frac{2}{1000} + \frac{M^v_{w,a}(x)}{M_{H_2}(x) + M^v_{w,a}(x)} \cdot \frac{18}{1000} \right) \cdot \frac{P_a(x)}{T_a(x) \cdot R_u} \tag{30}$$

$$\begin{aligned} \mu_a(x) = & \frac{M_{H_2}(x)}{M_{H_2}(x) + M^v_{w,a}(x)} \left[ \frac{T_a(x) - T_1}{T_2 - T_1} (\mu_{H_2,T_2} - \mu_{H_2,T_1}) + \mu_{H_2,T_1} \right] \\ & + \frac{M^v_{w,a}(x)}{M_{H_2}(x) + M^v_{w,a}(x)} \left[ \frac{T_a(x) - T_3}{T_4 - T_3} (\mu_{vap,T_4} - \mu_{vap,T_3}) + \mu_{vap,T_3} \right] \end{aligned} \tag{31}$$

Cathode:

$$\rho_c(x) = \left( \begin{aligned} & \frac{M_{O_2}(x)}{M_{O_2}(x) + M_{N_2}(x) + M^v_{w,c}(x)} \cdot \frac{32}{1000} + \frac{M_{N_2}(x)}{M_{O_2}(x) + M_{N_2}(x) + M^v_{w,c}(x)} \cdot \frac{28}{1000} \\ & + \frac{M^v_{w,a}(x)}{M_{O_2}(x) + M_{N_2}(x) + M^v_{w,c}(x)} \cdot \frac{18}{1000} \end{aligned} \right) \cdot \frac{P_c(x)}{T_c(x) \cdot R_u} \tag{32}$$

$$\begin{aligned} \mu_c(x) = & \frac{M_{O_2}(x)}{M_{O_2}(x) + M_{N_2}(x) + M^v_{w,c}(x)} \left[ \frac{T_c(x) - T_5}{T_6 - T_5} (\mu_{O_2,T_6} - \mu_{O_2,T_5}) + \mu_{O_2,T_5} \right] \\ & + \frac{M_{N_2}(x)}{M_{O_2}(x) + M_{N_2}(x) + M^v_{w,c}(x)} \left[ \frac{T_c(x) - T_5}{T_6 - T_5} (\mu_{N_2,T_6} - \mu_{N_2,T_5}) + \mu_{N_2,T_5} \right] \\ & + \frac{M^v_{w,c}(x)}{M_{O_2}(x) + M_{N_2}(x) + M^v_{w,c}(x)} \left[ \frac{T_c(x) - T_7}{T_8 - T_7} (\mu_{vap,T_8} - \mu_{vap,T_7}) + \mu_{vap,T_7} \right] \end{aligned} \tag{33}$$

The local volume flow rate $Q_k(x)$ could be calculated as follows.

Anode: $$Q_a(x) = \left(M^v_{w,a}(x) + M_{H_2}(x)\right) \cdot R_u \cdot \frac{T_a(x)}{P_a(x)} \tag{34}$$

Cathode: $$Q_c(x) = \left(M_{O_2}(x) + M_{N_2}(x) + M^v_{w,a}(x)\right) \cdot R_u \cdot \frac{T_c(x)}{P_c(x)} \tag{35}$$

### 4.5 Cell Potential and Current Density

The cell voltage $E_{cell}$ was determined from open circuit voltage $E_{oc}$, membrane resistance, current density and overpotentials [20]:

$$E_{cell} = E_{oc} - \eta_{act} - \eta_{ohmic} \tag{36}$$

where $\eta_{act}$ is activation loss associated with elctro-chemical reactions, and $\eta_{ohmic}$ is the loss from ohmic resistance in the membrane. The reversible open circuit voltage $E_{oc}$ was calculated from a modified form of the Nernst equation [21].

$$\begin{aligned} E_{oc}(x) = {} & 1.229 - 0.85\times10^{-3}(T_s(x) - 298.15) \\ & + 4.31\times10^{-5} T_s(x)\left[\ln\left(P^*_{H_2}(x)\right) + \frac{1}{2}\ln\left(P^*_{O_2}(x)\right)\right] \end{aligned} \tag{37}$$

where $T_s(x)$ is the local cell temperature, $P^*_{H_2}(x)$ and $P^*_{O_2}(x)$ are local effective surface partial pressures of hydrogen and oxygen in atmospheres (atm) [27] [28].

$$P^*_{H_2}(x) = P_a(x) - 0.5 \cdot P_{w,a}(x) \tag{38}$$

$$P^*_{O_2}(x) = P_c(x) - P_{w,c}(x) - P_{N_2}(x) \cdot \exp\left(\frac{0.291 \cdot I(x)}{T^{0.832}}\right) \tag{39}$$

Note that the exchange current density at cathode is much smaller than that at anode; therefore, the overpotential at the anode is negligible compared to that at the cathode. $\eta_{act}$ [18] and $\eta_{ohmic}$ could be calculated as follows.

$$\eta_{act}(x) = \frac{R[273 + T_s(x)]}{0.5F} \ln\left[\frac{P_c(x) \cdot I(x)}{I^0 \cdot P_{O_2}(x)}\right] \tag{40}$$

$$\eta_{ohmic}(x) = \frac{I(x) \cdot t_m}{\sigma_m(x)} \tag{41}$$

In a PEM fuel cell, the membrane acts as a separator as well an electrolyte. The membrane conductive $\sigma_m(x)$ is highly dependent on its hydration state. During operation, the net water flux is from anode to the cathode side, leading to membrane dehydration on the anode side and flooding on the cathode side with additional water from reaction production. Therefore, the membrane conductivity $\sigma_m(x)$, is a function of water content in the membrane. In most of literature, the water activity at the anode side or the average value between anode and cathode is used. The former is not physically reasonable and the

latter leads to much higher performance than experimental results. In the present model, an amendment was given for the water activity in the membrane. The combined effect of both sides was considered.

$$a_m = \beta \cdot a_a + (1-\beta) a_c \tag{42}$$

where $\beta$ could be adjusted based on the operating conditions. Knowing $a_m$, some formulae similar to (13) and (14) could be used to calculate $c_m(x)$. Then membrane conductivity could be evaluated as [7]:

$$\sigma_m(x) = \left( 0.00514 \frac{W_{m,dry}}{\rho_{m,dry}} c_m(x) - 0.00326 \right) \cdot \exp\left( 1268 \left[ \frac{1}{303} - \frac{1}{273 + T_s(x)} \right] \right) \tag{43}$$

### 4.6 Catalyst Layer Model

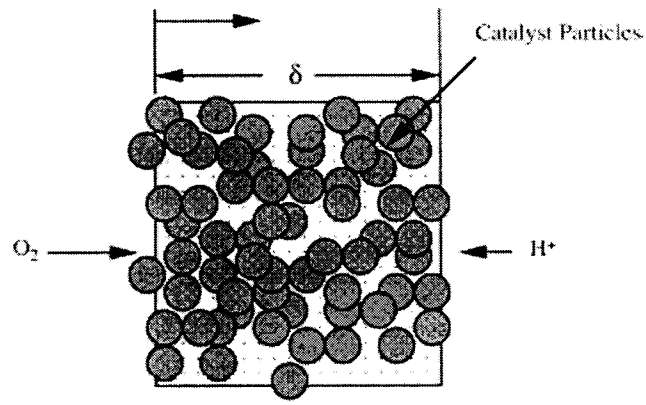


Fig. 4. Schematic of the catalyst layer [24]

The cathode catalyst layer is assumed consist of a mixture of catalyst platinum, ionomer membrane electrolyte, and void space. The small catalyst particles, either on their own or supported on relatively large carbon black particles, are covered by a thin, continuous layer of ionomer.

The positive direction points from the cathode electrode to the membrane with its origin located at the interface between the cathode electrode and catalyst layer. All fluxes are taken as positive in the positive $y$-direction, while the electric current density is opposite to the $y$-direction, as shown.

The void space is usually sufficiently large so that the Knudsen diffusion is unimportant compared to the bulk diffusion. The catalyst layer has a uniform distribution of its various components and a small thickness compared to its height and depth so that a one-dimensional approximation in the $y$-direction is made.

The ionomer layer surrounding the catalyst particles is taken to be fully hydrated, and the void region in the catalyst layer is assumed to be fully flooded.

The current density distribution [24]:

$$\frac{\partial I(x,y)}{\partial y} = A_v I_{0,ref}\left(\frac{C_{O_2}(x,y)}{C_{O_2,ref}}\right)^{\gamma}\left[\exp\left(\frac{\alpha_c F\eta(x,y)}{R_u T_s(x)}\right)-\exp\left(-\frac{\alpha_a F\eta(x,y)}{R_u T_s(x)}\right)\right] \tag{44}$$

The specific reaction surface area $A_v$ is given by:

$$A_v = \frac{m_{Pt}A_s}{\delta} \tag{45}$$

where $m_{Pt}$ is the catalyst mass loading per unit area of the cathode, $A_s$ is the catalyst surface area per unit mass of the catalyst, and $\delta$ is the thickness of catalyst layer. The catalyst surface area varies greatly for different types of supported catalysts and platinum black, as shown in Table 1.

$C_{O_2}$ is the concentration of oxygen, $C_{O_2,ref}$ is the reference concentration of oxygen, $\alpha$ is the transfer coefficient, $\eta(x,y)$ is the cathode overpotential, $T_s(x)$ is the temperature of the catalyst layer, $R_u$ is the universal gas constant. Typically, the reaction order $\gamma$ is usually taken as unity.

The experimental data of Parthasarathy *et al.* [29] were used to correlate the reference exchange current density for oxygen reduction in Nafion. The data were correlated with the cell temperature.

$$\log_{10}\left(I_{0.ref}\right) = 3.507 - \frac{4001}{T_s(x)} \tag{46}$$

where $I_{0,ref}$ is in A/cm$^2$, and temperature is in Kelvins.

The overpotential distribution [24]:

$$\frac{\partial \eta(x,y)}{\partial y} = \left(\frac{1}{k_m^{eff}} + \frac{1}{k_s^{eff}}\right) I(x,y) - \frac{1}{k_s^{eff}} I(x,\delta) \tag{47}$$

The effective electric and ionic conductivity are determined from the correlations accounting for the porous nature of the catalyst layer [30] similar to that for gas diffusion discussed earlier. They are:

$$k_m^{eff} = (l_m \phi_c)^{3/2} k_m \tag{48}$$

$$k_s^{eff} = (1-\phi_c)^{3/2} k_s \tag{49}$$

where $k_m$ and $k_s$ are the bulk conductivities of the ionomer and solid catalyst.

The ionomer loading $l_m$ of the catalyst layer is defined as the ratio of the volume occupied by the ionomer to the total void space available in the catalyst layer.

It should be noted that the void fraction $\phi_c$ is related to the type of catalyst, $m_{Pt}$ and $\delta$ as follows:

$$\phi_c = 1 - \left( \frac{1}{\rho_{Pt}} + \frac{1-\%Pt}{\%Pt\,\rho_c} \right) \frac{m_{Pt}}{\delta} \tag{50}$$

where $\%Pt$ represents the percentage of platinum catalyst on the carbon black support by mass, $\rho_{Pt}$ and $\rho_c$ are the densities of platinum and carbon black respectively. Therefore, for a given type of catalyst, only two out of the three parameters ($\phi_c$, $m_{Pt}$ and $\delta$) need to be specified and the third can be determined from Equation (50). For pure platinum, often called platinum black, $\%Pt$ = 100%. The void fraction is a macroscopic parameter representing the porous nature of the catalyst layer, although the microscopic characteristics of the layer may be very complex and difficult to describe exactly.

The equation for the oxygen concentration variation in the catalyst layer [24]:

$$\frac{\partial C_{O_2}(x,y)}{\partial y} = \frac{1}{4FD_{O_2}^{eff}}\left[I(x,y) - I(x,\delta)\right] \tag{51}$$

where the effective diffusion coefficient $D_{O_2}^{eff}$ is calculated from the bulk diffusion coefficient $D_{O_2}$, for oxygen diffusion through the void region of the catalyst layer and a correction factor to account for the non-diffusing space occupied by the solid catalyst particles [30].

$$D_{O_2}^{eff} = \phi_c^{3/2} D_{O_2} \tag{52}$$

The bulk $O_2$ diffusion coefficient can be expressed as follows:

$$D_{O_2} = \frac{D_{O_2-m} D_{O_2-H_2O}}{(1-l_m)D_{O_2-m} + l_m D_{O_2-H_2O}} \tag{53}$$

where $D_{O_2-H_2O}$ and $D_{O_2-m}$ are the diffusion coefficient of oxygen in liquid water and membrane.

$$D_{O_2-m} = -1.0664\times10^{-5} + 9.0215\times10^{-6} \times \exp\left(\frac{T_s(x) - 273.15}{106.65}\right) \tag{54}$$

Three boundary conditions are required for a unique solution. At the cathode electrode and catalyst layer interface, the protonic current must vanish as electrode is ionically insulated.

$$I(x,y) = 0 \text{ at } y = 0 \tag{55}$$

On the other hand, the protonic current density and overpotential at $y = \delta$ is equal to the local cell current density and overpotential, or

$$I(x,y) = I(x,\delta) \tag{56}$$

$$\eta(x,y) = \eta(x,\delta) \tag{57}$$

# 5. SOLUTION METHODOLOGY

The main focus of this chapter is how to build the simulation procedure based on the model discussed in precious chapters. For the integration of non-linear, second order differential equations, two options are available, namely, keeping constant voltage or keeping constant average current density. The author adopted the latter one in this work. The flow charts of the solution are as shown in Figs. 5,6,7.

## 5.1 The Convergence Criteria

For one unknown $x$, if $\left|\frac{x_i^{k+1} - x_i^k}{x_i^k}\right| < \varepsilon$ ($i$ = 1, 2, 3, 4....., stands for each unknown parameter, $k$ means iteration number), we treat it as a converged value. ($\varepsilon$ is convergence criteria which the precision is $10^{-5}$).

## 5.2 Numerical Methods Review

The set of nonlinear differential equations are used in the model, which include 13 governing equations and 13 unknown variables. It is know that all the main parameters in this model are coupled, if one parameter gets a change, all corresponding data will change simultaneously. Generally, the methods to solve nonlinear differential equations can be categorized into two groups: direct methods and indirect or iterative methods.

Direct method is quite straightforward, the relations between the variables are predefined, the unknown variables are formulated in term of known variables, once the

input values are known, the values of corresponding unknowns will be calculated by these predefined formulas. The classical direct method is Runge-Kutta method, which numerically integrates ordinary differential equations by using additional steps at the predicted mid-point of an interval to cancel out lower-order error terms. Therefore, this method is also called as "predictor-corrector algorithms".

Fourth-order Runge-Kutta formula is the classical method, which has a certain sleekness of organization. It requires four evaluations per step. The benefit of this method is that it is reasonably simple and robust. Runge-Kutta method, which is sometimes combined with an intelligent adaptive step-size routine, is a good candidate for numerical solution of differential equations.

The following equations are the formula of fourth-order Runge-Kutta method [31]:

$$\begin{aligned} x_{n+1} &= x_n + h \\ y_{n+1} &= y_n + \frac{1}{6}(k_1 + 2k_2 + 2k_3 + k_4) + O(h^5) \end{aligned} \tag{58}$$

where

$$\begin{aligned} k_1 &= hf(x_n, y_n) \\ k_2 &= hf(x_n + \frac{1}{2}h, y_n + \frac{1}{2}k_1) \\ k_3 &= hf(x_n + \frac{1}{2}h, y_n + \frac{1}{2}k_2) \\ k_4 &= hf(x_n + h, y_n + k_3) \end{aligned} \tag{59}$$

At step $n$, the value of current point $x_n$, $y_n$ and the interval between the current point and next point $h$ are already known. Function $f(x, y)$ can evaluate the slope of solution curve at a particular point $(x, y)$. According to Euler method $y = hf(x, y)$, a $y$-direction

jump value can be derived. At step $n+1$, $x_{n+1}$ can be simply attained by add step interval $h$. However, the value of $y_{n+1}$ in $y$-direction is much more complex to decide. In the above formula, $k_1$ means $y$-direction jump from the current point to the next Euler-predicted point; $k_2$ is far more interesting. Here, we also use Euler's method to predict a mid-point which lies half-way across the predicted interval. The value of this predicted mid-point in $x$ direction is $x_n + h/2$, and $y_n + k_1/2$ in $y$ direction. Recalling that function $f(x, y)$ means the slope of solution curve, $hf(x_n + \frac{1}{2}h, y_n + \frac{1}{2}k_1)$ give us the second $y$-direction jump $k_2$; Similarly, $k_3$ is the third $y$-direction jump, but instead of using $k_1$, we use the $k_2$ to predict the $y$-value of the mid-point; $k_4$ is the jump value which is based on the predicted right end-point of the interval. As before, the $y$-value of this predicted point is decided by $k_3$. Once all the four jump values in $y$-direction have been calculated, a weighted average formula is used to evaluate the $y_{n+1}$. To analysis the algorithm, if we can generalize the direct methods by using $y_{n+1} = c\, y_n$, where $c$ is a coefficient that depends upon the method used and the equation being evaluated. The primary reason, which makes the fourth order Runge-Kutta method successful, is that the coefficient $c$ that it produces is almost always a very precise approximation to the actual value [5].

Compare to direct method, iterative methods are relatively easy for programming, and use less computer memory than the direct methods. The tradeoff of iterative method calculation is that it will take longer time to repeat the same calculations in each recursion. Unlike the direct methods which are always try to find an exact solution to the equations system, iterative methods attempt to find the solution by repeatedly solving the equations system by using approximations to the vector. Iterations continue until the solution is within a predetermined acceptable bound on the error. For the linear equations

system, well-known examples of this kind of algorithm include Gauss-Jacobi, Gauss-Seidel and Tri-diagonal matrix methods. For non-linear equations system, Newton-Raphson method is a commonly used algorithm. The disadvantages of iterative methods are: the total number of operations, typically on the order of $N$ per iteration cycle, cannot be predicted in advance; in addition, it is hard to guarantee the convergence unless the equations system satisfies fairly strict criteria. The main advantage of iterative methods is that only non-zero coefficients of the equations need to be stored in core memory. A brief explanation of each of these methods is listed as the following [5].

1. Gauss-Jacobi iteration can be expressed as [32]:

$$\vec{x}_{n+1} = D^{-1} \cdot \vec{b} - D^{-1} \cdot (L+U) \cdot \vec{x}_n \tag{60}$$

where $D$ is strictly diagonal matrix, $\vec{b}$ and $\vec{x}_n$ are known, and $D^{-1}\cdot(L+U)$ just scales the each row of the sum $(L+U)$ by the reciprocal of the corresponding element of $D$. Since the Gauss-Jacobi algorithm uses all values from the previous iteration, it has the disadvantage of slow convergence.

2. Gauss-Seidel iteration can be written as [32]

$$(D+L) \cdot \vec{x}_{n+1} + U \cdot \vec{x}_n = \vec{b} \tag{61}$$

where $x_{n+1}$ can be computed quite easily with simple forward substitution because $(D+L)$ is a lower triangular matrix. The practical advantage of this method over the

Gauss-Jacobi algorithm is that as soon as an element of the new solution vector at the iteration $n+1$ has been calculated, it can be used successively for the calculation of the remaining elements of $x_{n+1}$. Compared with the Gauss-Jacobi algorithm, which only uses elements calculated at the iteration $n$ to approximate the solution at iteration $n+1$, the Gauss-Seidel iteration converges twice as fast as Gauss-Jacobi in the average [5].

3. Tri-Diagonal Matrix Algorithm (TDMA) [33]: Gauss-Jacobi and Gauss-Seidel iterative methods are easy to implement, but they can be very slow to converge especially when the system of equations is large. In many real situations, the equations system can be simplified and described in form of tri-diagonal matrix, which means there are only nonzero elements on the diagonal, sub-diagonal and super-diagonal of matrix. Neither Gauss-Jacobi method nor Gauss-Seidel methods has any special treatments to make use of this special situations to improve their performance. Therefore, much computational time is wasted on the calculation of a full matrix, most of these calculations result in zero. In 1949, Thomas developed a technique for rapidly solving tri-diagonal system which is now called the Thomas Algorithm or the Tri-Diagonal Matrix Algorithm (TDMA). TDMA try to solve these sparsely populated matrices matrix system which have the equations in the form of $Ax=b$, where $x$ and $b$ are vectors, and $A$ is a tri-diagonal matrix. Basically, the TDMA follows the rule of the Gaussian elimination. In a full-matrix Gaussian elimination, TDMA eliminates all values below the main diagonal, solve the final equation, and then use that value in back-substitution to solve the remaining equations. For an $n$-dimensional matrix $A$, instead of storing a matrix of $n^2$, we need store just three $n$-dimensional vectors. In summary, by eliminating the unnecessary zero items

in the matrix $A$, TDMA can save computational time and use less system memory, which eventually leads to the improvement of the efficiency [5].

4. Newton-Raphson Algorithm [34]: Newton-Raphson method is one the most powerful methods in solving the nonlinear equations system. It is a root-finding algorithm that uses the first few terms of the Taylor series of a function $f(x)$ in the vicinity of a suspected root. The Taylor series of $f(x)$ about the point $x=x_0+\varepsilon$ is given by

$$f(x_0+\varepsilon)=f(x_0)+f'(x_0)\varepsilon+\frac{1}{2}f''(x_0)\varepsilon^2+... \tag{62}$$

Keeping the term only to the first-order, the above equation can be simplified as:

$$f(x_0+\varepsilon)\approx f(x_0)+f'(x_0)\varepsilon \tag{63}$$

in which, $\varepsilon$ means the offset between the root and an initial guess values $x_0$. For a given initial guess value $x_0$, $\varepsilon_0$ can be estimated as $\varepsilon_0=-\frac{f(x_0)}{f'(x_0)}$. After that, the method refines the guessed value as $x_1=x_0+\varepsilon_0$, and uses this value to get another $\varepsilon_1$. So on and so forth, the algorithm repeats the same process until it converges to a root using $\varepsilon_n=-\frac{f(x_n)}{f'(x_n)}$ [5].

In this study, fourth-order Runge-Kutta and Tri-Diagonal Matrix Algorithm are combined together to solve the one order and second order differential equations because

of the advantages discussed above. Newton-Raphson method is chosen to calculate the local current density and cell voltage. The mathematical model is implemented in a Java program on the Solaris platform with friendly Graphic User Interface. For a better understanding of solution procedure, the flow charts of the solution procedure are shown in Fig. 5 and Fig. 6.

### 5.3 Method for Unsteady State [35]

Parameters will change with the time in unsteady state. The standard discretised form for unsteady problem is [35]:

$$\begin{aligned} a_P T_P = {} & a_W\left[\theta T_W + (1-\theta)T_W^0\right] + a_E\left[\theta T_E + (1-\theta)T_E^0\right] \\ & + \left[a_P^0 - (1-\theta)a_W - (1-\theta)a_E\right]T_P^0 + b \end{aligned} \tag{64}$$

The exact form of the final discretised equation depends on the value of $\theta$. When $\theta$ is zero, we only use temperatures $T_P^0, T_W^0, T_E^0$ at the old time level $t$ on the right hand side of the equation to evaluate $T_P$ at the new time; the resulting scheme is called explicit. When $0 < \theta \le 1$ , temperatures at the new time level are used on both sides of the equation; the resulting scheme is called implicit. The case corresponding to $\theta = 1/2$ is called the Crank – Nicolson scheme.

Explicit scheme – The right hand side of the equation only contains values at the old time step so the left hand side can be calculated by forward marching in time. The scheme is based on backward differencing and its Taylor series truncation error accuracy

is first-order with respect to time. The inequality sets a stringent maximum limit to the step size and represents a serious limitation for the explicit scheme. It becomes very expensive to improve spatial accuracy because the maximum possible time step needs to be reduced as the square of space step. Consequently, this method is not recommended for general transient problems. Nevertheless, provided that the time step is chosen with care, the explicit scheme is efficient for simple problems.

Crank – Nicolson scheme – This method results from setting $\theta = 1/2$, the discretised equation is [35]:

$$a_P T_P = a_E\left[\frac{T_E + T_E^0}{2}\right] + a_W\left[\frac{T_W + T_W^0}{2}\right] + \left[a_P^0 - \frac{a_E}{2} - \frac{a_W}{2}\right]T_P^0 + b \qquad (65)$$

Since more than one unknown value of $T$ at the new time level is present in this equation, the method is implicit and simultaneous equations for all node points need to be solved at each time step. The time step limitation is less restrictive than that associate with the explicit method. The Crank - Nicolson method is based on central differencing and hence it is second-order accurate in time. With sufficient small time steps it is possible to achieve considerably greater accuracy than with the explicit method. The Crank - Nicolson scheme is normally used in conjunction with spatial central differencing.

In this study, the Crank - Nicolson scheme is chosen for unsteady case simulation. The time step $\Delta t = 0.5$ second is used in the dynamic calculations, thus changes of all the parameters could be traced at each half second. To make a clear understanding of the procedure, the flow chart of the solution procedure is shown in Fig. 7.

### 5.4 Parameters Used in Simulation

Channels are in rectangle shape and the co-flow configuration is used. The typical dimensions and parameters used for the simulations are listed in Table 2.

In this paper, the new concept "relative water content, $\phi$" is proposed, which is very useful for water analysis along the flow channel.

$$\phi = \frac{mole\ number\ of\ water\ (vapor + liquid)}{mole\ number\ of\ water\ vapor\ at\ saturation} \tag{66}$$

$$\phi_k(x) = \frac{\left(M^l_{w,k}(x) + M^v_{w,k}(x)\right)}{M_{gas,k}(x) \cdot \dfrac{P^{sat}_{w,k}(x)}{P_k(x)}} \tag{67}$$

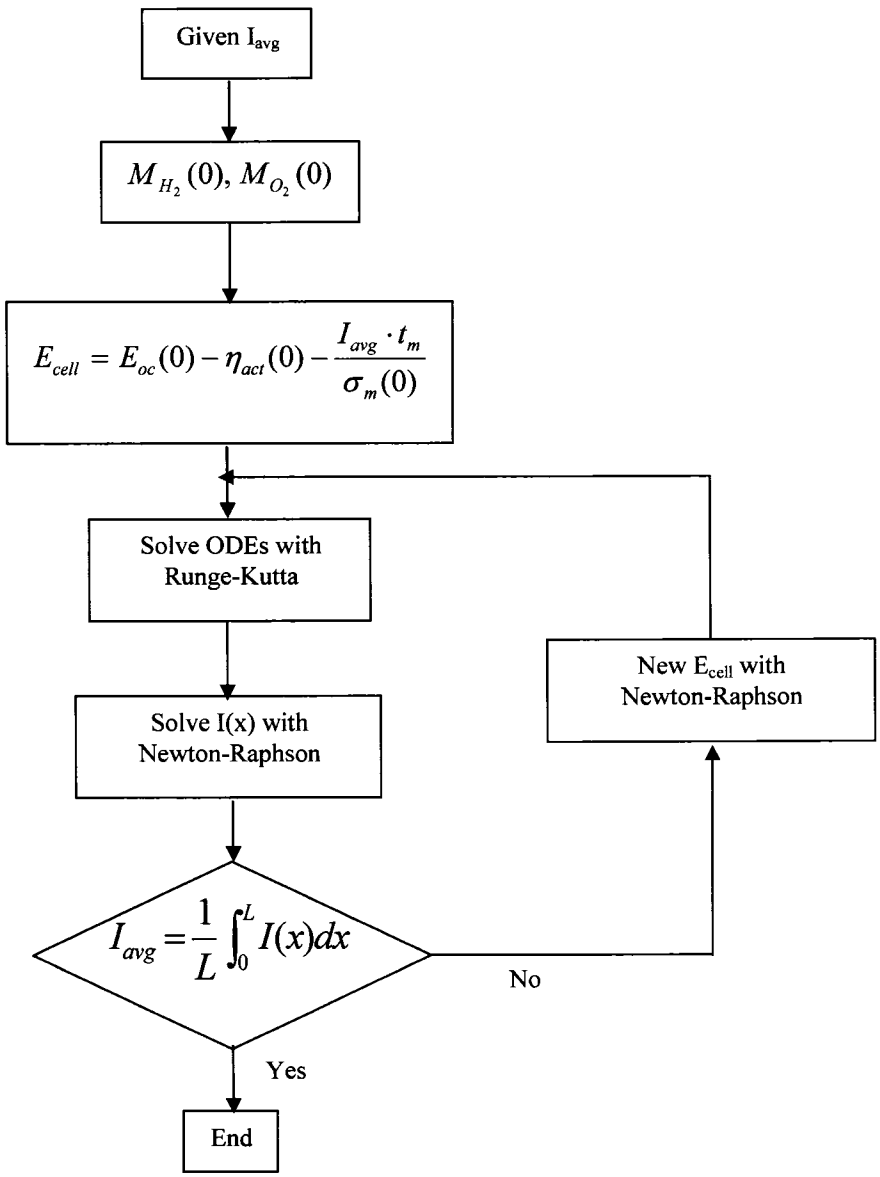


Fig. 5. Flow chart for steady state simulation with constant stack temperature

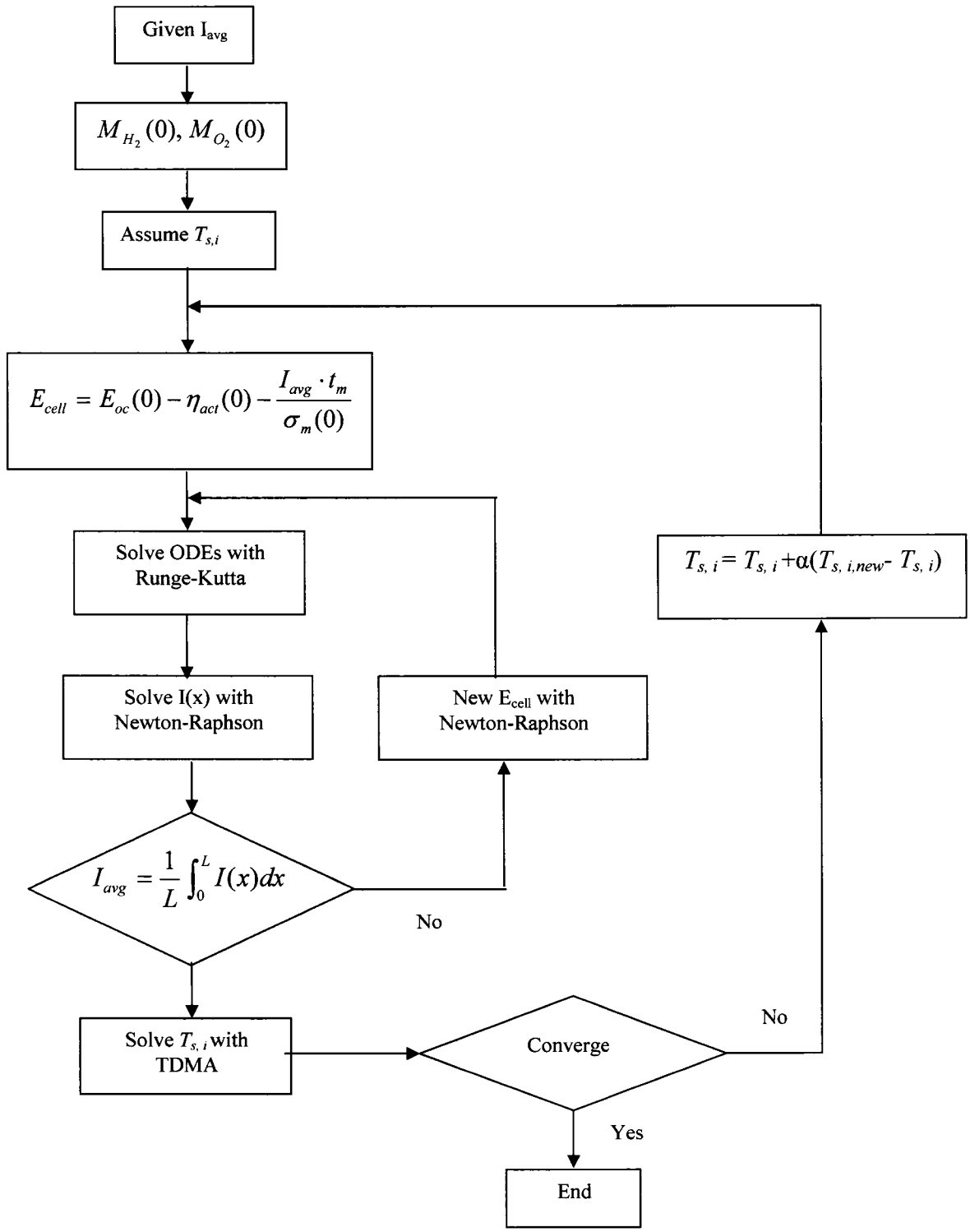


Fig. 6. Flow chart for steady state simulation with variable stack temperature

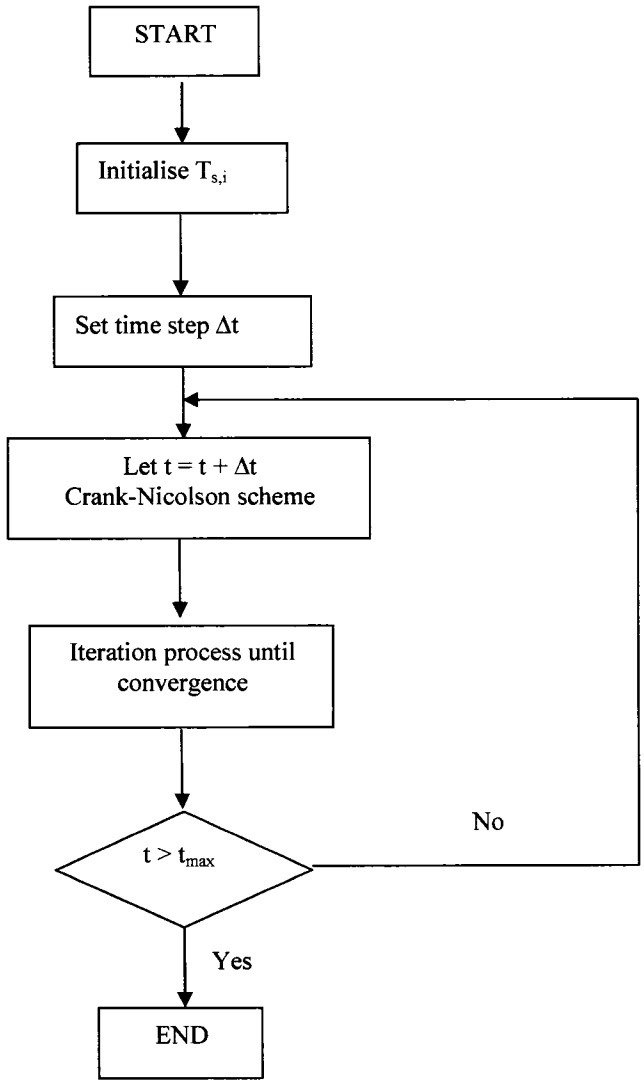


Fig. 7. Flow chart for unsteady state simulation

# 6. RESULTS AND DISCUSSIONS

## 6.1 Validation of the Model

Model validation is conducted here by comparing our simulation results with the experimental results from other group [36]. Fig. 8 shows a comparison of the simulation result from the present model (solid line) with the experimental data based on the similar operating condition (air is applied as oxidant; Nafion 115 membrane; hydrogen and air inlet pressure: 1.34 atm; hydrogen and air inlet temperature: 70°C). It can be seen that the prediction of the present model is in reasonable agreement with the experimental results.

From the figure, when the current density is less than 0.5 $A/cm^2$, the output voltage in the model is greater than experiment results. After the current density exceeds this value, the output voltage in the model is less than the experiment results. It means that the inner resistance in the model is greater than that in practice. Some factors may contribute to the error of the resistance calculation, which lead to the above simulation result.

In addition, for most operating region, the performance prediction by the variable stack temperature model (solid line) is better than that by the constant stack temperature model (dash-dot line).

Because the experimental facility is too complex and some information is not available, to get a more matched simulation with the experiment, we need to improve our model based on each specified experimental environment. Nevertheless, in this research, we'll use current model for further discussion since its prediction follows the same

tendency as the experimental data. As the same time, its prediction has an acceptable accuracy for qualitative analysis.

## 6.2 General Performance Analysis

*Effect of anode inlet humidification*

Fig. 9 shows the cell potential as a function of current density (the polarization curve) for different values of anode inlet relative water content with saturated cathode inlet gas. Fuel cell voltage increases as the anode inlet relative water content increases. Proper liquid water injection at the anode inlet is essential to supplement water vapor to the anode side. Higher water content of membrane because of higher inlet relative water content would lead to lower membrane resistance, which means the ohmic loss would be reduced. It should be mentioned that at low current density, the cell performance is kinetically controlled [7], which means that there would be no significant difference for different water content.

*Effect of pressure difference*

From the above analysis, net water molecule flux in the membrane arise from three mechanisms: electro-osmotic drag, which is caused by proton transport from the anode side to the cathode side of the membrane; back-diffusion by the concentration gradient of water between the anode side and the cathode side; and convection by water vapour pressure gradient between the anode side and cathode side. At lower current densities, back-diffusion water from the cathode to the anode side may be sufficient to maintain the

membrane well hydrated. But at the higher current densities, back-diffusion water is not sufficient to replenish the water loss because of electro-osmotic drag. Under this condition, the convection by pressure gradient could be used. With the anode gas inlet pressure maintain at 1 atm, three cathode inlet pressure levels are chosen, 1 atm, 2 atm and 3 atm. Other conditions are identical. Fig. 10 shows the effect of different pressure difference on the fuel cell performance at various current densities. Higher pressure difference leads to higher cell performance over the entire range of investigated current densities. The increase of cell performance by increasing the cathode inlet pressure from 1 atm to 2 atm is larger than that by increasing from 2 atm to 3 atm. The effect is more significant at higher current densities. This is because that the membrane is better hydrated with more water convection from cathode side to anode side, which yields lower ohmic loss. At higher current densities, electro-osmotic drag is higher, water convection plays more important role.

*Effect of temperature*

Fig. 11 shows the polarization curves for different cell temperatures. For lower current density, the flow rates of reactants and water are very small. The open circuit voltage dominates the cell voltage. Therefore, higher cell temperature leads to lower cell voltage. This is because the open circuit voltage decreases with the increase of cell temperature, which can be seen from Equation (37). For higher current density, it shows that fuel cell voltage increases with the increase of cell temperature. Higher temperature would lead to more inlet water with fixed inlet relative water content. The

water content in the membrane would increase consequently, which increases the membrane conductivity. However, cell temperature should not be higher than 373K [22].

*Effect of membrane thickness*

Fig. 12 shows the polarization curves for different membrane thickness. Fuel cell performance increases with the decrease of membrane thickness. This is because the ohmic loss decreases with decrease of distance traveled by hydrogen ions across the membrane. Therefore, a thinner membrane would produce better cell performance. However, the difficulty of preparing membrane electrode assemble using thin membrane should be considered [22].

*Effect of excess hydrogen and oxidant*

Fig. 13 shows the polarization curves for two oxidant gas compositions (pure oxygen and air) with different excess coefficients for hydrogen. Higher oxidant gas composition enhance the fuel cell voltage and maximum current density, therefore using pure oxygen instead of air as the oxidant would enhance overall performance. Higher $H_2$ excess coefficient would increase concentration of $H_2$ resulting in a further increase in cell performance. It should be noted that at low current density, cell performance is kinetically controlled and thus almost no perceivable difference in performance would be observed for different $H_2$ concentrations.

### 6.3 Influence of Inlet Water Content and Along Channel Analysis

Because the membrane performance and water transport are mainly controlled by the water content of anode side. In this section, we focus on the influence of anode inlet water content.

Fig. 14 shows the effect of anode inlet water content on the membrane conductivity. For the same cathode inlet water, the membrane conductivity increases with the anode inlet water content especially near the inlet, because higher anode inlet water leads to better hydrated situation. In anode channel, the liquid water will evaporate to generate water vapor.

Fig. 15 shows the local current density profiles with various anode inlet relative water contents when cathode inlet water content is fixed at 1.0. At the front part of the channels, the membrane is well hydrated, which leads to high membrane conductivity and high local current density. The water content of anode side dominates the membrane performance. Therefore, the current density increases with anode inlet relative water content near the inlet up to the inlet with saturation condition. In Fig. 15, comparing the two cases of $\phi_{a,in}$=1.0 and $\phi_{a,in}$=1.1, it can be found that if liquid water is supplied ($\phi_{a,in}$=1.1), the current density is a little lower near the inlet. This is because the change of membrane conductivity due to the liquid water ($\phi_{a,in}$=1.1) is very small near the inlet, while the cell voltage for $\phi_{a,in}$=1.1 is higher than that of saturation condition ($\phi_{a,in}$=1.0) at inlet (Fig. 16). In the downstream channel, the membrane conductivity is better because of the evaporation of liquid water, so the current density is a little higher than that with saturation condition at inlet. The membrane performance and water transport are mainly controlled by the water content of anode side.

Fig. 17 shows the anode inlet water effect on the activation loss. In the front part of the channel, the activation loss increases with anode inlet water up to saturation, which agrees with the local current density discussed in Fig. 15. In the rear part of the channel, the effect is reversed due to the combined effects of temperature, local current density and partial pressure of oxygen.

For Fig. 14, Fig. 15 and Fig. 17, there are some common characteristics for these figures. Near the inlet of fuel cell, $\phi_{a,in}$ plays an important role, especially when $\phi_{a,in}$ <1. Along the channel in the main flow direction, this effect decreases. This is because the water content of anode side decreases along the channel due to water transportation from anode side to cathode side, while water content of cathode side increases due to water transportation from anode to cathode and reaction production inside cathode. The effects of water content of cathode side on membrane performance increases. For the curve with $\phi_{a,in}$ of 1.1, a sudden change at the position of $x$ around 90% of channel length is observed since there is no more liquid water thereafter to evaporate.

Fig. 18 shows the effect of anode inlet water contents on the ohmic loss. Increased amount of inlet water leads to lower ohmic loss. This is because the increased amount of inlet water leads to a higher membrane conductivity as shown in Fig. 14, which dominates the ohmic loss although the higher inlet water contents leads to higher current density in certain area as shown in Fig. 15. The ohmic loss profile along the flow channel depends on the combined effects of local current density and membrane conductivity, which can be seen from Equation (41).

Fig. 19 shows the effect of anode inlet water content on the net water flux per proton. Near the inlet, the net water flux is higher due to high electro-osmotic drag

coefficient near the anode inlet. The net water flux increases with anode inlet water content, which is because the higher anode water content provides higher electro-osmotic drag coefficient as shown in Fig. 20.

Fig. 21 and Fig. 22 show the effect of anode inlet water content on the partial pressure of hydrogen and oxygen along the channel. The main reason for the increase of the partial pressure of hydrogen is that anode vapor pressure decreases more rapidly than hydrogen. The higher the anode inlet water is, the lower the partial pressures are for both hydrogen and oxygen. For hydrogen, higher anode inlet water leads to higher partial pressure of water vapor, which decreases the partial pressure of hydrogen.

The partial pressure of oxygen decreases along the channel because of the depletion of oxygen and the increase of cathode water vapor pressure, which is shown in Fig. 24. The partial pressure of oxygen decreases rapidly near the inlet because of the higher depletion rate of oxygen due to the higher local current density (Fig. 15) in this region. For oxygen, higher anode inlet water leads to higher water vapor transportation across the membrane that leads to lower oxygen partial pressure. Once the anode inlet has reached saturation condition, its effect on the partial pressure of oxygen is very small because the water vapor of anode side is enough for the requirement of transportation and the liquid water evaporates very slowly under this condition. Therefore, the increase of water vapor on anode side because of liquid water evaporation almost has no effect on the pressure of cathode side.

Fig. 23 shows the effect of anode inlet water content on the water vapor partial pressure along the anode channel. The vapor pressure decreases along anode channel due to the water transportation across the membrane from anode to cathode side. At the front

section of the channel, the vapor pressure decreases rapidly. This is because that the membrane is well hydrated near the inlet, which leads to higher electro-osmotic drag coefficient ($n_d$) and net water flux per proton ($\alpha$).

Fig. 24 shows the effect of anode inlet water content on the water vapor partial pressure along the cathode channel. The vapor pressure increases along cathode channel due to water transportation and electrochemical reaction. Increased anode inlet water content corresponds to increased vapor pressure for both sides.

Fig. 25 shows the effect of anode inlet water content on the liquid water mole number in anode channel. It is clear that there would be no liquid water in anode if the anode inlet water content is less or equal to one. When $\phi_{a,in}$ >1.0, in anode channel, the liquid water decreases along the channel since it evaporates to supplement vapor continuously. With $\phi_{a,in}$ =1.1, the liquid water disappears at the position of $x$ around 90% of channel length. There is no more liquid water thereafter to evaporate.

In Fig. 26, the liquid water in cathode channel increases along the channel since vapor condenses to liquid due to more water supplied by reaction. The increased anode inlet water amount corresponds to higher liquid water on the cathode side due to water transport across membrane from anode side to cathode side. Once the anode inlet reach saturation, such effect of the liquid water is very small as shown in the figure for $\phi_{a,in}$ =1.0, 1.1 and 1.25.

Reynolds number is one of the important parameters in fluid flow. Fig. 27 shows the effects of anode inlet water contents on the Reynolds number at cathode along the channel. Reynolds number increases in cathode because viscosity decreases, velocity increases as shown in Fig. 28 and density does not change much along the channel as

shown in the authors' previous research [26]. The larger the inlet water content, the larger the velocity and Reynolds number in cathode flow channel. For the present studies, the flow is obviously in laminar flow regime. In Fig. 28, the gas velocity increases along cathode flow channel due to water transportation and electrochemical reaction product. Higher anode inlet water content yields higher gas velocity in cathode channel because of water transport from anode side to cathode side.

The pressure loss cannot be neglected and it is one of the important parameters for fuel cell system design especially for cathode channel with air as oxidant instead of pure oxygen. Fig. 29 shows the local pressure in cathode along the channel. The local cathode pressure varies almost linearly. The greater the inlet water amount, the larger the pressure drop. The pressure drop in cathode is around 8000 Pa, which is very close to practical operating situation, e.g., the Nexa$^{TM}$ Ballard PEM fuel cell operated here in our laboratory.

The pressure drops for different control volumes are not equal. The local pressure drop increases because volume flow rate increases. The required pumping power for cathode increases with the increase of the length of channel, which is shown in Fig. 30. The greater the inlet water content at anode and cathode, the larger the pumping power required. Four channels are applied for the present study. The total pumping power for cathode flow of a single cell is proportional to the number of channels.

Fig. 31 shows the effects of pressure loss in the flow channel and anode inlet water content on the power of single fuel cell. It can also be seen that when the pressure loss is considered, the cell power is lower than that without considering the pressure drop. The most important reason is that the pressure loss decreases the partial pressure of oxygen,

which leads to higher activation loss. In addition, the pressure loss decreases the water content in the membrane, which decreases the membrane conductivity and increases the ohmic loss. In the case the average current density is fixed, the higher the anode inlet water content ($\phi_{a,in}$ = 0.5 ~ 1.25), the higher the fuel cell power, i.e., the fuel cell performance can be improved by humidifying the anode. Also injecting certain amount of liquid water into anode inlet could improve the fuel cell output power. Table 3 gives the detailed information of this effect. It can be seen that the percentage of the power loss due to the pressure drop increases with the decrease of anode inlet water content. The lower the fuel cell power is, the higher this percentage is.

Fig. 32 shows the gas temperature distributions in the anode flow channel, cathode flow channel and the stack temperature. At the vicinity of the inlet, heat can be transferred from the stack to the environment by the convection, which leads to the stack temperature lower than the stream temperature. The stack temperature heats up quickly because the higher gas temperatures and the energy released by reactions. Further down to the channel, there are several heat transfer processes took place: (i) chemical reaction occurs and reaction heat is released to the solid stack. (ii) water vapor condenses and latent heat is released. (iii) convection heat transfer occurs as well since the temperature difference between the stream and stack. According to the curve, the anode and cathode gas temperatures drop quickly near the inlet of channels. When they reach the stack temperature, they increase with stack temperature. In the downstream channel, the anode and cathode gas temperatures stay very close to the solid temperature except that stack temperature drops rapidly near the outlet as more energy is transferred from the stack to the surroundings [20].

Fig. 33 shows the contribution of each water transport mechanism, including net water flux per proton ($\alpha$), electro-osmotic drag coefficient ($n_d$), diffusion part by concentration gradient of water vapor and convection part by water vapor pressure gradient. The contribution of convection part looks like zero in the figure just because the value is too small. Near the inlet of fuel cell, the electro-osmotic drag coefficient ($n_d$) and net water flux per proton ($\alpha$) is higher because the membrane is well hydrated, as mentioned earlier. Diffusion is from anode to cathode side in this region, and then from cathode to anode side, since the water concentration of anode side decreases and that of cathode side increases along the flow channel. This is because that the water transfer across membrane due to diffusion effect is purely dependent on the water concentration gradient across the membrane. It could be back-diffusion only if the water concentration at cathode is higher than that in anode as usually it does.

Fig. 34 shows the local relative water content ($\phi$), water activity ($a$) and relative humidity ($RH$) along the anode flow channel. The $a_a$ (dotted) is hidden by $RH$ (solid) since $RH$ equals to $a$ if $a \leq 1$. Water vapor decreases along the anode channel as the water vapor is transported across the membrane along the channel from anode to cathode side. Because the partial pressure of water vapor is less than saturation pressure in the channel, the liquid water would evaporate to generate water vapor, and water activity and relative humidity would have the same value. At the position of 90% of length, evaporation process is complete and all the liquid water in the channel have been utilized and the three curves merge. The region between solid line and dashed line represents liquid water and that below the solid line represents water vapor, as shown in Fig. 34.

Fig. 35 shows the local relative water content ($\phi$), water activity ($a$) and relative humidity ($RH$) along the cathode flow channel. There are three sources of water in cathode channel; one is water transferred from the anode side, the second is water from reaction products, and the third is the water carried from the cathode inlet. The three curves start from the same point of 0.5. Water vapor increases along the cathode channel. The region between "$a$" and "$\phi$" represents liquid water and that below "$a$" represents water vapor. Note that water activity could be greater than one, especially if the condensation rate is less than the overall effect of production and transportation. Because the partial pressure of water vapor is greater than saturation pressure in the channel, the water vapor would condense to generate liquid water.

### 6.4 Catalyst Layer Analysis

This model combined the along-flow-channel model and the catalyst layer model. Instead of the published catalyst layer model with the main assumption of the uniform performance along flow channel, the local parameters along the flow channel are applied, which is closer to the real case. As well known, the catalyst layer is situated between the electrode and membrane. In a typical PEM fuel cell, the catalyst layer is composed of a porous mixture of platinum, often supported with a carbon substrate, ionomer and Teflon binder. This region is the heart of the fuel cell [37]. The simulation result and analysis can be very useful for the catalyst layer design and optimization, such as composition, platinum loading and so on.

To solve the set of governing differential equations, a four order Runge – Kutta method is chosen. The catalyst layer has a thickness of 5.0 μm and platinum loading of 4.0 mg/cm$^3$. The operation conditions are listed in Table 2. Fig. 36 shows a typical result for the distribution of the current density within the cathode catalyst layer. At the front part of the flow channels, the membrane is well hydrated, which leads to high membrane conductivity and high local current density. At the interface between cathode electrode and catalyst layer (y = 0), the current density is equal to zero as electrode is ionically insulated [24]. The current density at the membrane boundary is equal to the output current density of the cell. It can be seen from the figure that current density increases rapidly near the electrode boundary (y = 0). The current density reaches the cell current density at the location that the oxygen concentration vanishes as shown in Fig. 38.

Fig. 37 shows a result for the distribution of the overpotential within the cathode catalyst layer. The overpotential is normalized by the value at membrane boundary and inlet of the flow channel. The figure shows that the variation of overpotential is quite small within the catalyst layer as compared with the oxygen concentration and current density. Fig. 38 shows the distribution of the oxygen concentration within the catalyst layer. The oxygen concentration is normalized by the value at electrode boundary and inlet of the flow channel. The oxygen concentration decreases along the flow channel because of the depletion of oxygen and the increase of water vapor. The oxygen concentration decreases rapidly near the inlet of the flow channel because of the higher depletion rate of oxygen due to the higher local current density in this region. Along the direction across the catalyst layer, it is seen from the figure that the oxygen concentration decreases rapidly since the current density increases rapidly in this region. At the inlet of

the flow channel, the oxygen concentration vanishes at the position of about 40% of the catalyst layer thickness. This zero oxygen concentration location moves towards the electrode boundary along the flow channel since depletion of oxygen.

### 6.5 Unsteady State Analysis

The dynamic response of fuel cell is important for vehicular applications since the fuel cell does not usually operate at the optimal steady state designed by the fuel manufacturer. The dynamics of PEM fuel cells are complex and include the mass transport of materials through the membrane and to and from the electrodes, reaction mechanisms and rates at the electrodes, voltages and currents produced depending on the pressures, temperatures and concentrations at the electrodes, overpotential and Ohmic loss throughout the process. The implicit Crank – Nicholson method is used, in which the partial differential equation is discretized, resulting in a system of algebraic equations that defines the dependence between the stack temperature profiles and consecutive times [38].

In this study, the system transient phenomena is computed starting from a uniform solid temperature of 25°C using the data from the base case. Fig. 39 shows the evolution of average stack temperature with time. And the evolutions of stack temperature profiles with time (t = 2.5 s, t = 5.0 s, t = 7.5 s, t = 10 s, t = 15 s, t = 20 s and t = 25 s) are shown in Fig. 40. It can be seen from the two figures that the system settles well inside 25 seconds.

Fig. 41 and Fig. 42 show the evolutions of the pressure drop in the anode and cathode flow channels with time. With the increase of temperature, the volume flow rate increases, resulting in higher gas velocity in the flow channel, which leads to higher pressure drop on both anode side and cathode side. Fig. 43 shows the evolution of pumping power at cathode side with time. The pumping power increases with time since the same transient tendency of pressure drop. Only the pumping power on cathode side is shown here since the pressure drop on cathode side is significant. Fig. 44 and Fig. 45 show the evolutions of average membrane conductivity and activation loss with time. The membrane conductivity is based on the combined effects of stack temperature and water activity in the membrane, which can be seen from Equation (43). From Fig. 45, it can be seen that the activation loss increases with time before the fuel cell system settles. Low stack temperature will cause a slow electrochemical reaction; as a result, the cell output voltage will be reduced. Increased stack temperature does speed up the reaction and reduce activation loss, however there is negative effect. It will enhance the partial pressure of water vapor inside the flow channel. For an inlet pressure fixed channel, it will reduce the partial pressure of the reactants. Base on Equation (40), the activation loss increases with stack temperature. In general, the dynamic simulation results are very important for the fuel cell system control.

# 7. CONCLUSIONS AND RECOMMENDATIONS

## 7.1 Conclusions

In this study, a steady and unsteady, water and thermal management model was developed, which considers pressure effect, pressure drop, open circuit voltage dependence on pressure and stack temperature, and membrane conductivity dependence on the water vapor from both anode and cathode sides. It is shown that the present model agreed reasonably with the experimental results and has sufficient accuracy for engineering applications.

The model can predict a series of important parameter profiles along the flow channel; current density, overpotential and oxygen concentration distributions in the catalyst layer can be calculated. Transient phenomena of the PEM fuel cell can be simulated with this model as well. This model can be used as part of a PEM fuel cell stack or system modeling.

In addition, a new concept of relative water content was proposed; this concept is useful for identifying liquid water and water vapor along the flow channels. Through this parameter, the water flow rate and its phase (liquid or vapor) can be identified easily by reading the curves. Thus it provides an easy way to classify the state of water that is very important for the designers when they propose a new design.

The effects of various operating and design parameters on fuel cell performance were investigated. The effects of anode inlet relative water contents on the fuel cell

performance were also investigated. In addition, the simulations for unsteady state were conducted. Based on this study, the following conclusions can be drawn:

1. The humidification of both anode and cathode is very important for the performance of PEM fuel cell. The water content of anode side, which tends to dry, dominates membrane performance and plays a key role on the performance of PEM fuel cell. When inlet humidification is applied to improve cell performance, the increase of pumping power and burden of water removal because of humidification should also be considered in the system design.
2. Proper liquid water injection at anode inlet could improve fuel cell performance since the liquid water could evaporate to generate water vapor and thus to make the membrane well hydrated. The liquid water injection at cathode inlet is not advocated because it would not improve the cell performance but increase the burden of water removal.
3. The PEM fuel cell performance could be improved by increasing the flow inlet temperatures within a reasonable range (should not be higher than 373K).
4. Higher pressure difference between cathode and anode side leads to higher fuel cell performance.
5. The pressure drop in the PEM fuel cell flow channels increases the pumping power cost. So it must be paid more attention when designing a fuel cell, especially air is used other than pure oxygen. Pressure loss is one of the important parameters that affect total system efficiency and optimization.
6. The dynamic simulation results are very important for the fuel cell system control.

## 7.2 Recommendations for Future Work

It is recommended that future work be conducted in term of the following aspects:

1. The model presented here should be validated through systematic experimental investigation.
2. The liquid water behavior in the flow channels and two-phase flow may be introduced into this model to simulate the phase change more precisely.

## REFERENCES


[1] Kenny, Michael, Presentation at the Fuel Cell Vehicle Technology Conference, UC Davis, Davis, CA, 1998.

[2] A. Bauen, and D. Hart, Assessment of Environmental Benefits of Transport and Stationary Fuel Cells, Journal of Power Sources, 86 (2000) 482-494.

[3] CARB, Proposed Amendments to the California Zero Emission Vehicle Program Regulations, 2000.

[4] T. Woegerer, Research, design and construction of proton exchange membrane fuel cell. E.S.419-Project report, the University of Western Ontario, 1998.

[5] Y. Zong, Water and Thermal Management in a Single PEM Fuel Cell, Thesis for MASc Degree, University of Windsor, 2005.

[6] J. Larminie, A. Dicks, Fuel Cell Systems Explained. John Wiley & Sons, Ltd., 2002.

[7] T. Nguyen, R. White, A water and heat management model for proton-exchange-membrane fuel cells, Journal of the Electrochemical Society, 140(8) (1993) 2178-2186.

[8] P. Badrinarayanan, PEM fuel cell water and thermal management: A methodology to understand water and thermal management in an automotive fuel cell system, Birla Institute of Technology and Science, Pilani, India, 1999.

[9] J. Larminie, A. Dicks, fuel cell systems explained, second edition, (2003), 72-75.

[10] X. Yu, Water and Thermal Management of PEM Fuel Cell Stack, Thesis for MASc Degree, University of Windsor, 2005.

[11] P. Costamagna and S. Srinivasan, Quantum jumps in the PEMFC science and technology from the 1960s to the year 2000 Part II. Engineering, technology development and application aspects, Journal of Power Sources, 102 (2001) 253-269.

[12] K. Yao, K. Karan, K. McAuley, P. Oosthuizen, B. Peppley, and T. Xie, A review of mathematical models for hydrogen and direct methanol polymer electrolyte membrane fuel cells, Fuel Cells, 4 (1-2) (2004) 3-29.

[13] M. Verbrugge, R. Hill, Ion and Solvent Transport in Ion-Exchange Membranes I. A Macrohomogeneous Mathematical Model, Journal of the Electrochemical Society, 137(3) (1990) 886-895.

[14] M. Verbrugge, R. Hill, Transport phenomena in perfluorosulfonic acid membranes during the passage of current, Journal of the Electrochemical Society, 137(4) (1990) 1131-1138.

[15] D. Bernardi, M. Verbrugge, Mathematical model of a gas-diffusion electrode bonded to a polymer electrolyte, AIChE Journal, 37 (8) (1991) 1151-1163.

[16] D. Bernardi, M. Verbrugge, A mathematical model of the solid-polymer-electrolyte fuel cell, Journal of the Electrochemical Society, 139(9) (1992) 2477-2491.

[17] T. Springer, T. Zawodzinski, S. Gottesfeld, Modeling water content effects in polymer electrolyte fuel cells in: White R, Verbrugge M, Stockel J (Eds.). Modelling of batteries and fuel cells, 91(10): 209-223, The Electrochemical Society, Softbound Proceedings Series, Pennington, NJ, 1991.

[18] T. Springer, T. Zawodzinski, S. Gottesfeld, Polymer electrolyte fuel cells model, Journal of the Electrochemical Society, 138(8) (1991) 2334-2342.

[19] T. Fuller, J. Newman, Water and thermal management in solid-polymer-electrolyte fuel cells, Journal of the Electrochemical Society, 140(5) (1993) 1218-1225.

[20] J. Yi, T. Nguyen, An along-the-channel model for proton exchange membrane fuel cells, Journal of the Electrochemical Society, 145(4) (1998) 1149-1159.

[21] C. Marr, X. Li, An engineering model of proton exchange membrane fuel cell performance, ARI. 50 (1998) 190-200.

[22] S. Ge, B. Yi, A mathematical model for PEMFC in different flow models, Journal of Power Sources, 124 (2003) 1-11.

[23] S. Maharudrayya, S. Jayaanti, Pressure losses in laminar flow through serpentine channels in fuel cell stacks, Journal of Power Sources, 138 (2004) 1-13.

[24] C. Marr, X. Li, Composition and performance modelling of catalyst layer in a proton exchange membrane fuel cell, Journal of Power Sources, 77 (1999) 17-27.

[25] R. Felder, R. Rousseau, Elementary Principles of Chemical Processes, John Wiley & Sons, Inc., 1978.

[26] B. Zhou, Y. Zong, Relative humidity effects on the flow in PEM fuel cell cathode, CSME Forum, S-7, 2004.

[27] J. Amphlett, R. Baumert, R. Mann, B. Peppley, P. Roberge, Performance modeling of the Ballard Mark IV solid polymer electrolyte fuel cell, Journal of the Electrochemical Society, 142(1) (1995) 1-8.

[28] J. Amphlett, R. Baumert, R. Mann, B. Peppley, P. Roberge, Performance modeling of the Ballard Mark IV solid polymer electrolyte fuel cell, Journal of the Electrochemical Society, 142(1) (1995) 9-15.

[29] A. Parthasarathy, S. Srinivasan, J. Appleby, Temperature dependence of the electrode kinetics of oxygen reduction at the platinumrNafion interface—a microelectrode investigation, J. Electrochem. Soc., 139 (9) (1992) 2530–2537.

[30] R.E. De la Rue, C.W. Tobias, On the conductivity of dispersions, J. Electrochem. Soc., 106 (1959) 827–833.

[31] http://calculus.sjdccd.cc.ca.us/ODE/7-C-3/7-C-3-h.html

[32] http://www.exp-math.uni-essen.de/~ajung/diplom/

[33] http://mathworld.wolfram.com/NewtonsMethod.html

[34] http://www.enseeiht.fr/hmf/travaux/CD0001/travaux/optmfn/hi/01pa/hyb74/node24.html

[35] H. K. Versteeg, W. Malalasekera, An introduction to computational fluid dynamics, The finite volume method, Longman Group Ltd., 1995.

[36] L. Wang, A. Husar, T, Zhou, H. Liu, A parametric study of PEM fuel cell performances, International Journal of Hydrogen Energy, 28 (2003) 1263-1272.

[37] C. Marr, Performance modeling of a proton exchange membrane fuel cell, Thesis for MASc degree, University of Victoria, 1989.

[38] J. Golbert, D. R. Lewin, Model-based control of fuel cells: (1) Regulatory control, Journal of Power Sources, 135 (2004) 135-151.

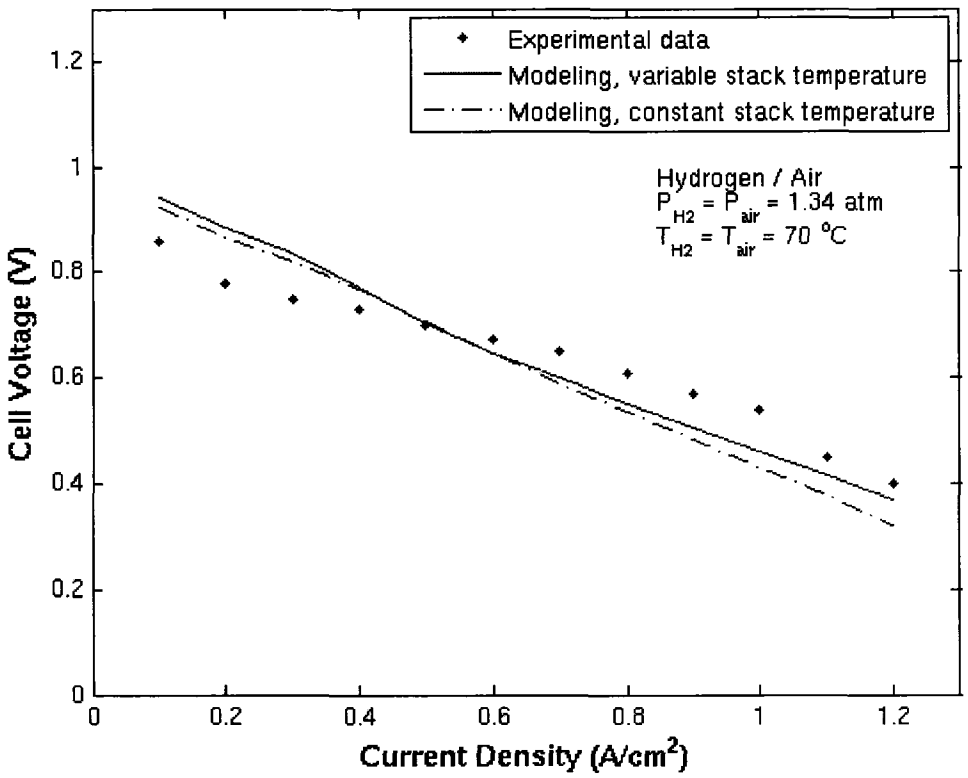


Fig. 8. Comparison between the numerical results and experimental data

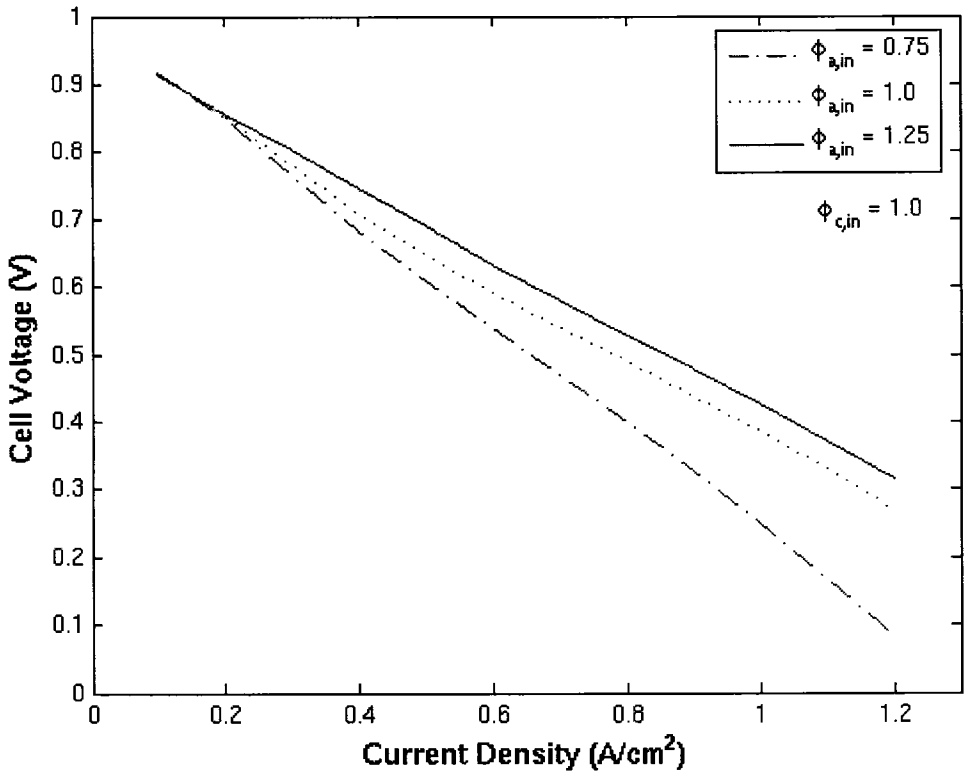


Fig. 9. Effect of anode inlet humidification on cell performance (hydrogen/air)

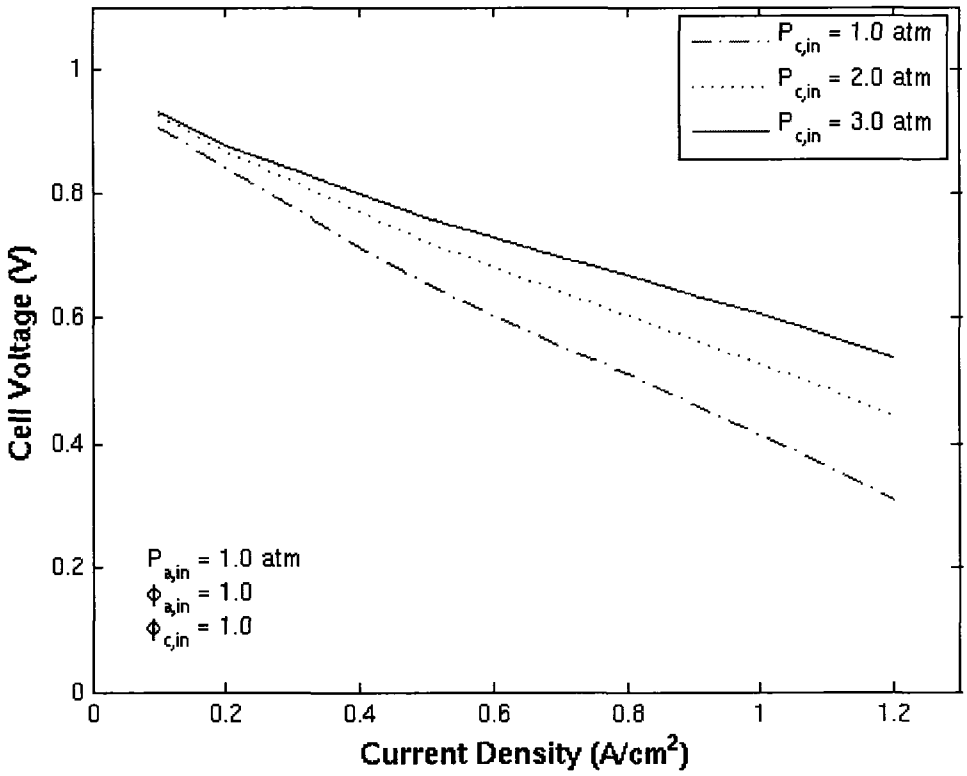


Fig. 10. Effect of pressure on cell performance (hydrogen/air)

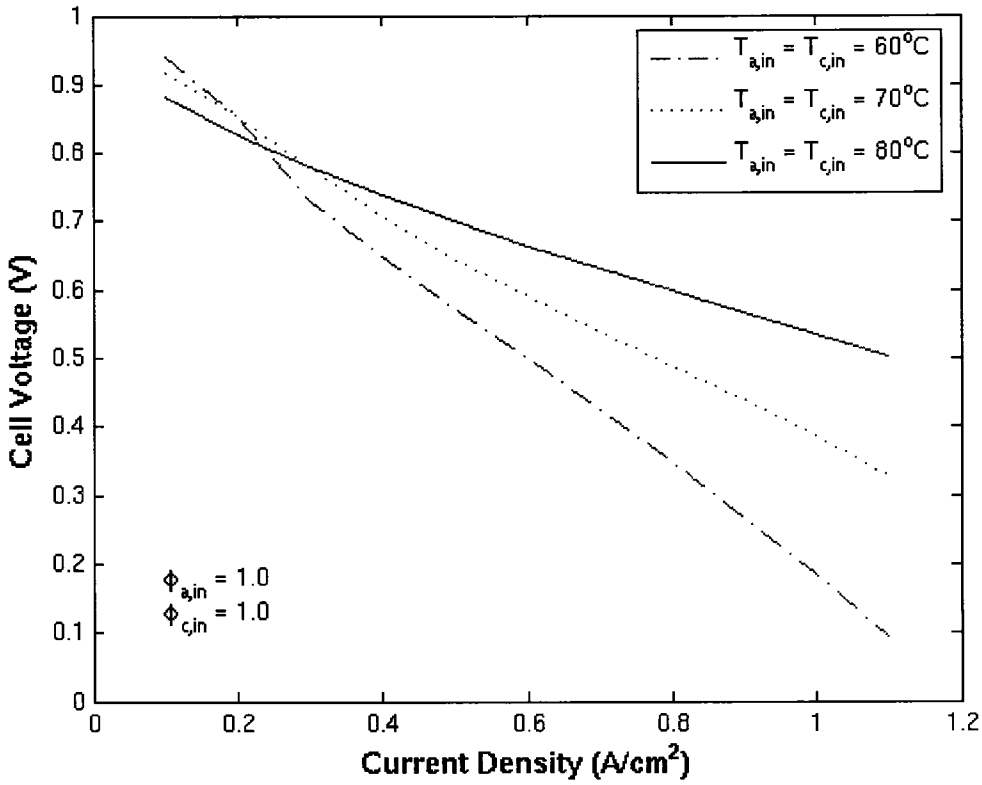


Fig. 11. Effect of cell temperature on cell performance (hydrogen/air)

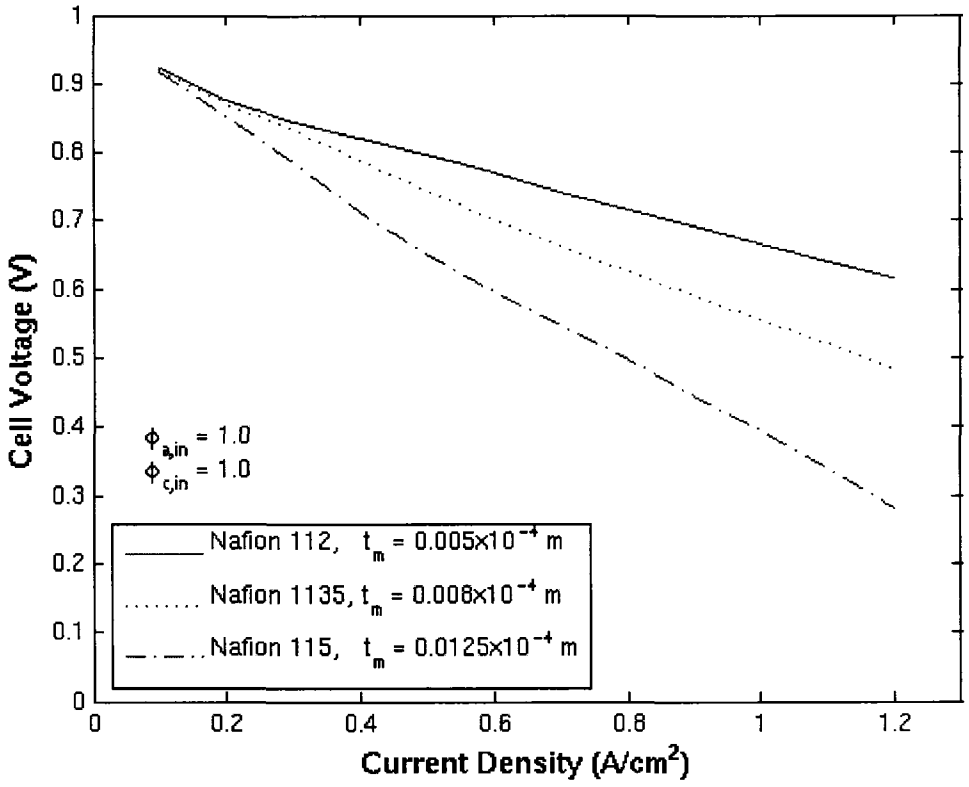


Fig. 12. Effect of membrane thickness on cell performance (hydrogen/air)

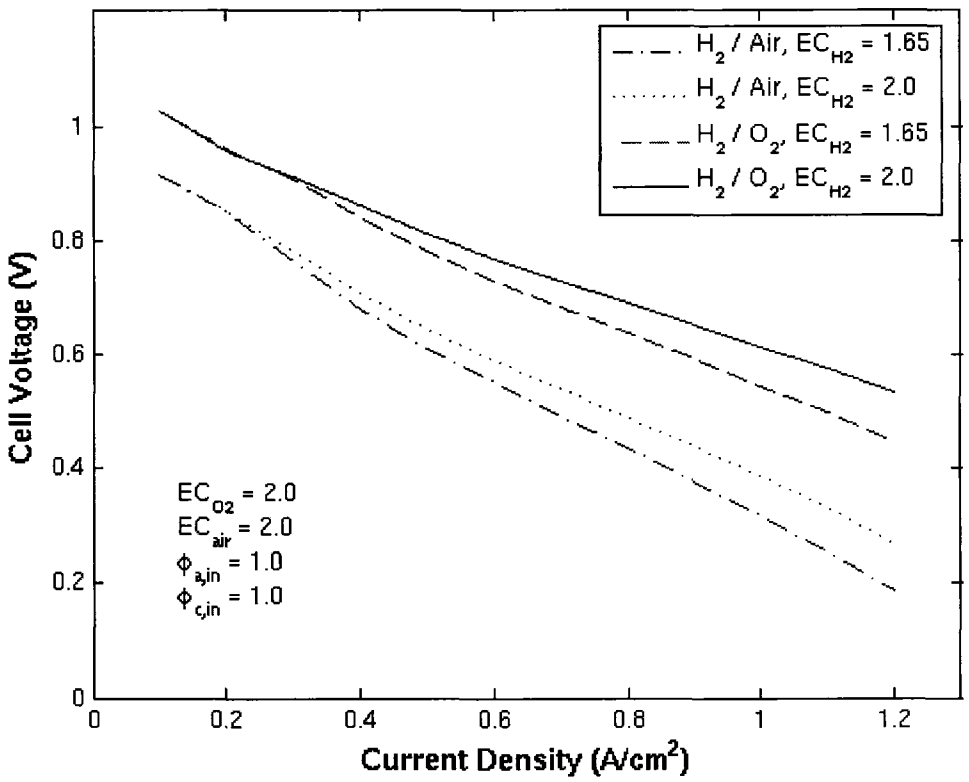


Fig. 13. Effect of oxidant and excess hydrogen on cell performance

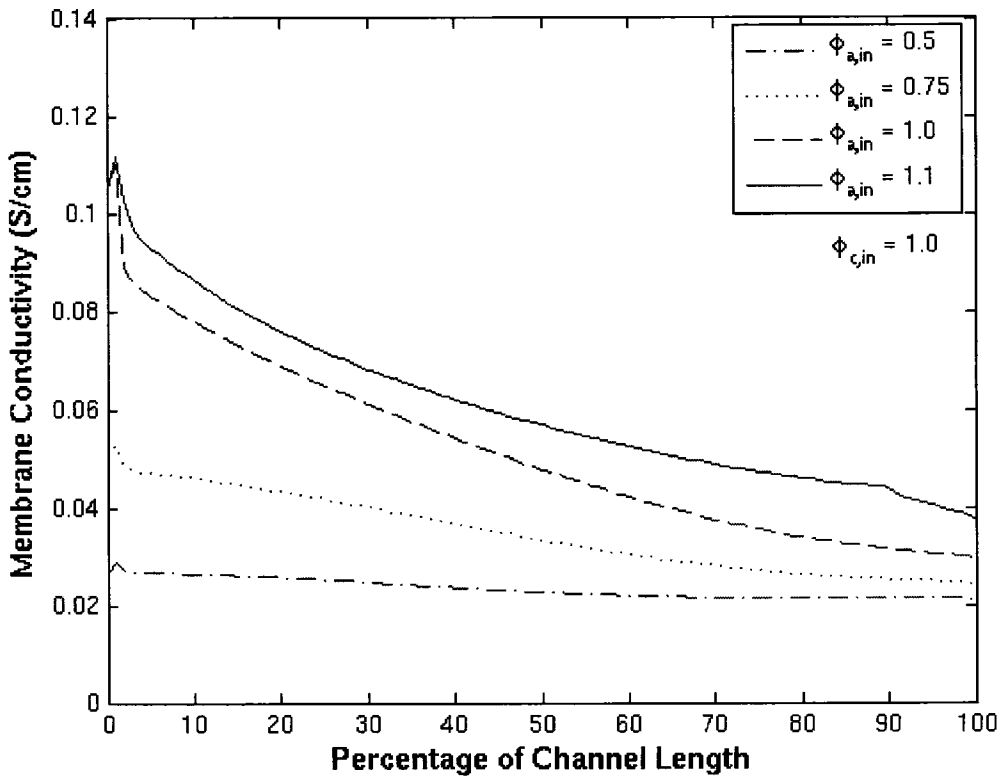


Fig. 14. Effect of anode inlet water content on the membrane conductivity

(Pure oxygen; $\phi_{c,in} = 1.0$; $\phi_{a,in} = 0.5, 0.75, 1.0, 1.1$)

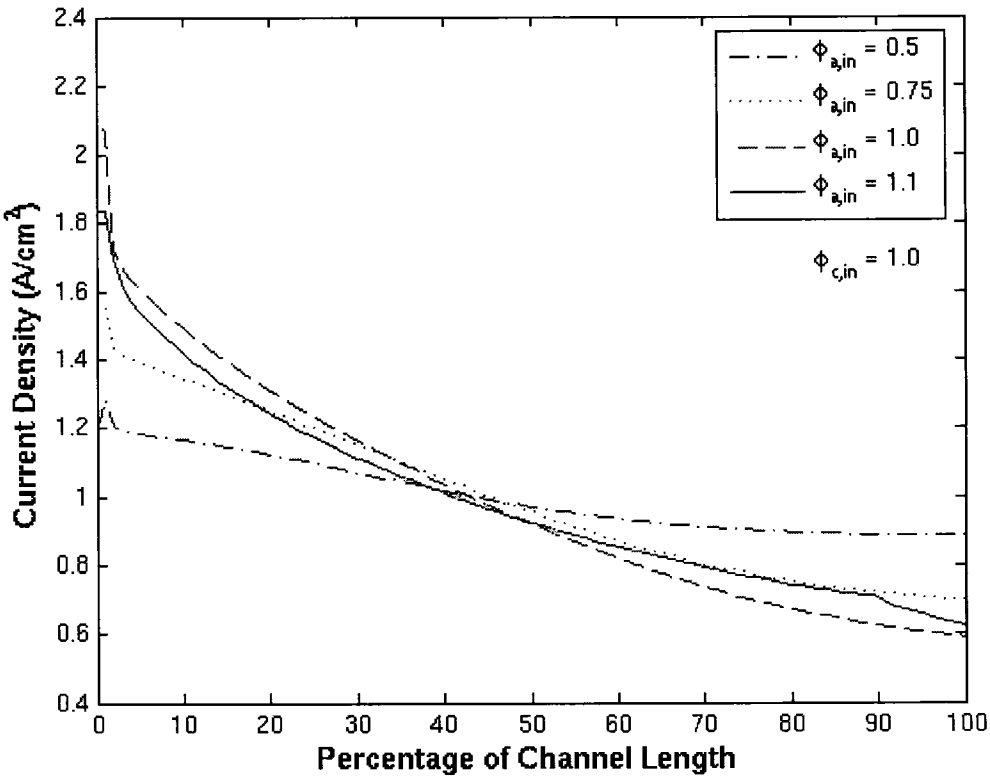


Fig. 15. Effect of anode inlet water content on the current density

(Pure oxygen; $\phi_{c,in}$ = 1.0; $\phi_{a,in}$ = 0.5, 0.75, 1.0, 1.1)

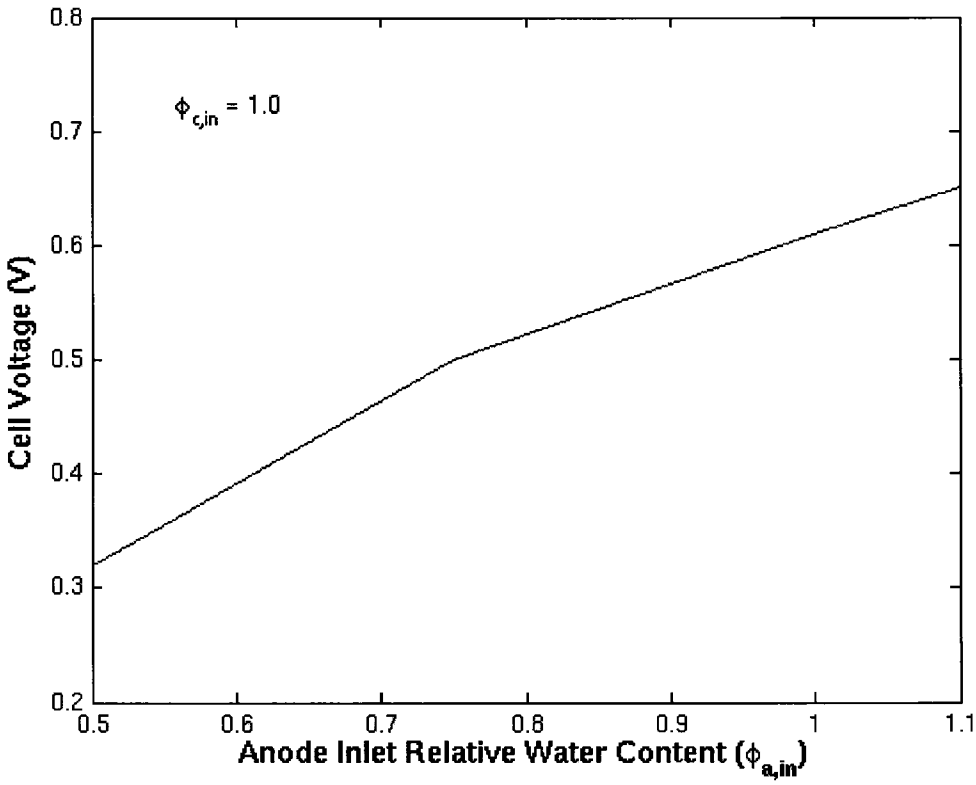


Fig. 16. Effect of anode inlet water content on the cell voltage (Pure oxygen)

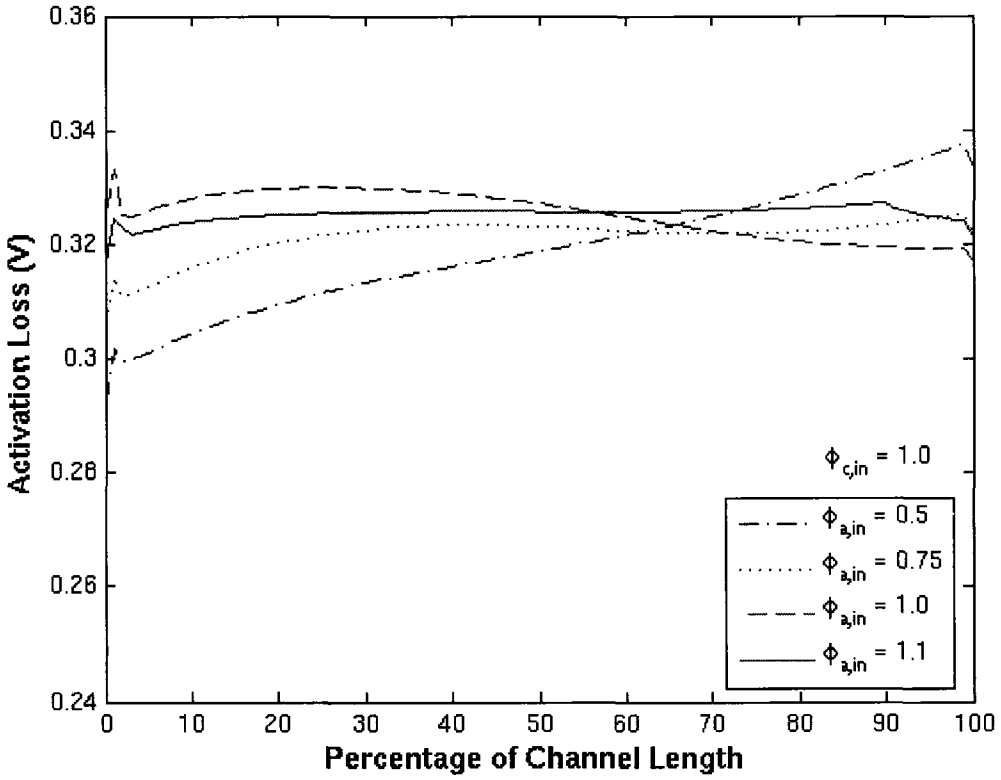


Fig. 17. Effect of anode inlet water content on the activation loss

(Pure oxygen; $\phi_{c,in} = 1.0$; $\phi_{a,in} = 0.5, 0.75, 1.0, 1.1$)

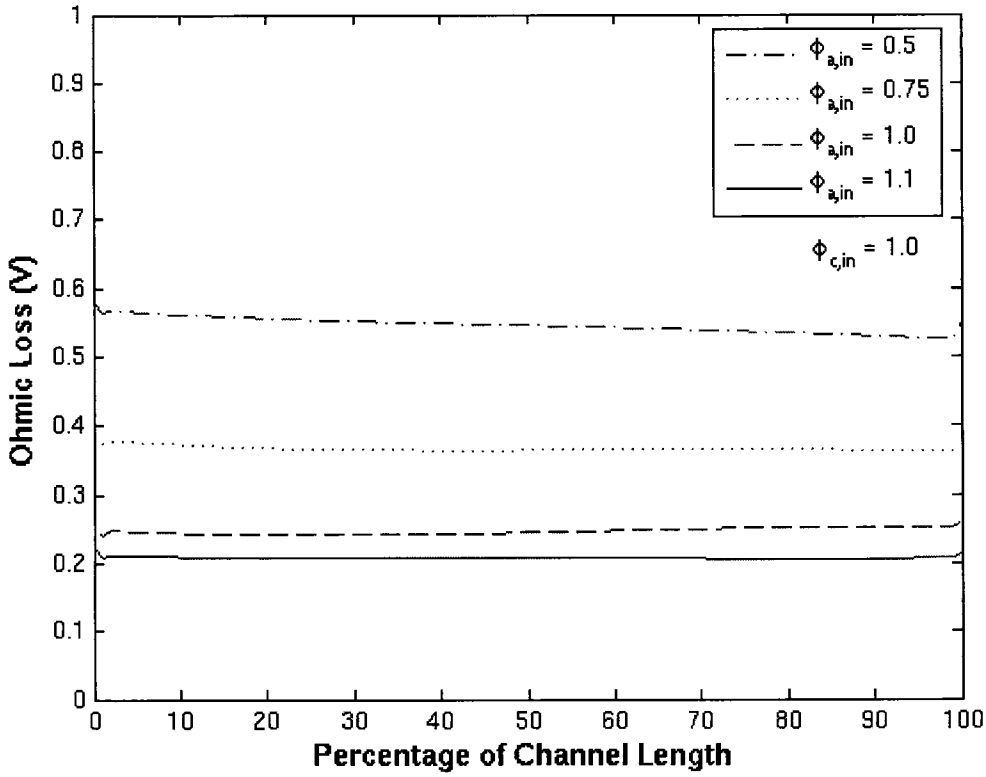


Fig. 18. Effect of anode inlet water content on the ohmic loss

(Pure oxygen; $\phi_{c,in}$ = 1.0; $\phi_{a,in}$ = 0.5, 0.75, 1.0, 1.1)

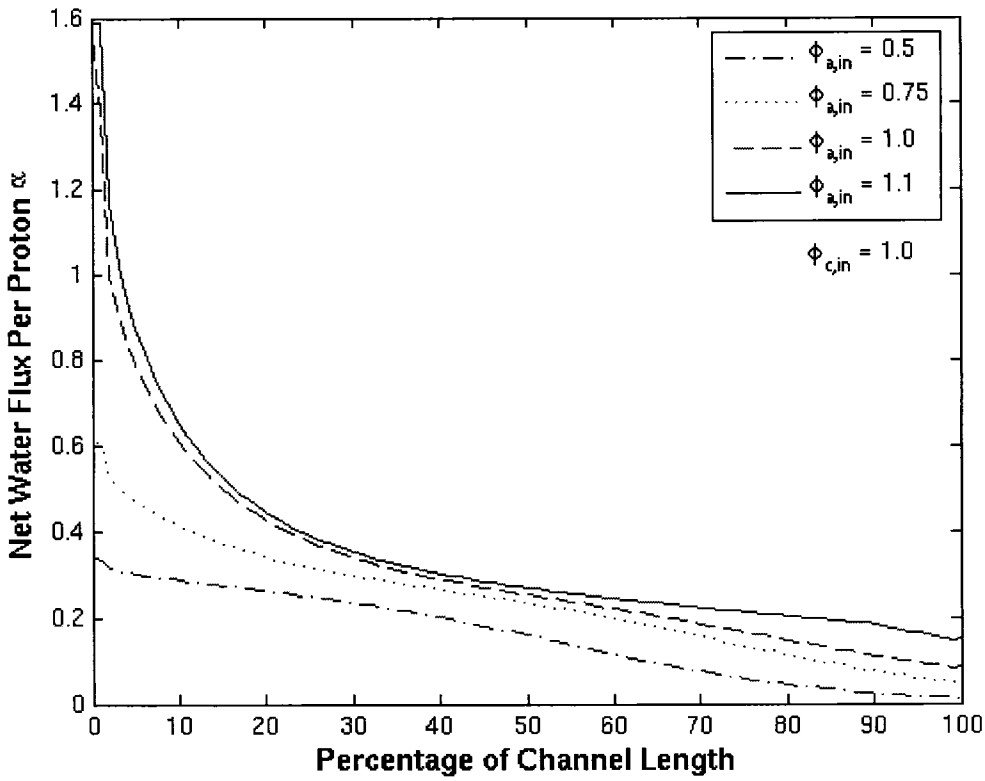


Fig. 19. Effect of anode inlet water content on net water flux per proton

(Pure oxygen; $\phi_{c,in}$ = 1.0; $\phi_{a,in}$ = 0.5, 0.75, 1.0, 1.1)

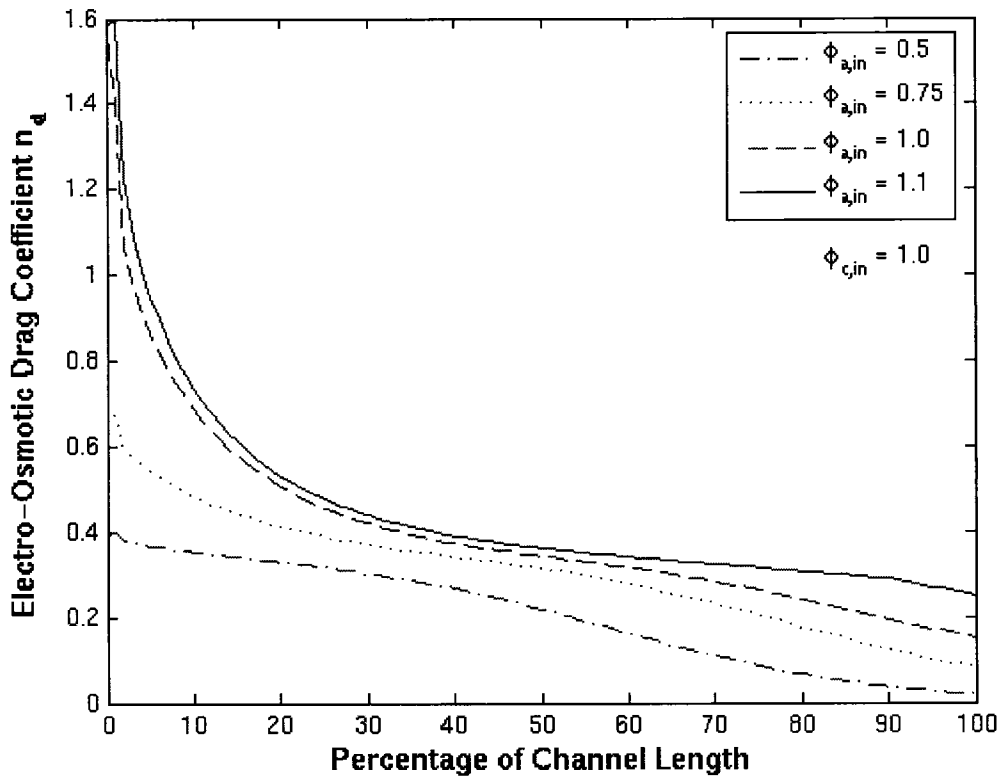


Fig. 20. Effect of anode inlet water content on electro-osmotic drag coefficient

(Pure oxygen; $\phi_{c,in}$ = 1.0; $\phi_{a,in}$ = 0.5, 0.75, 1.0, 1.1)

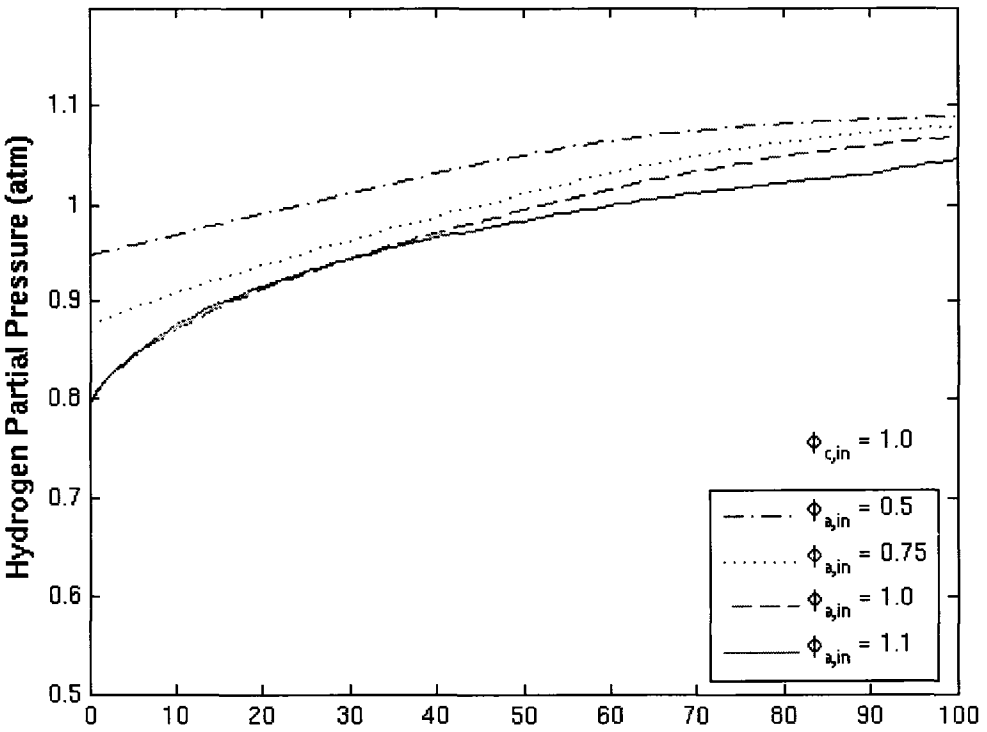


Fig. 21. Effect of anode inlet water content on the partial pressure of hydrogen

(Pure oxygen; $\phi_{c,in} = 1.0$; $\phi_{a,in} = 0.5, 0.75, 1.0, 1.1$)

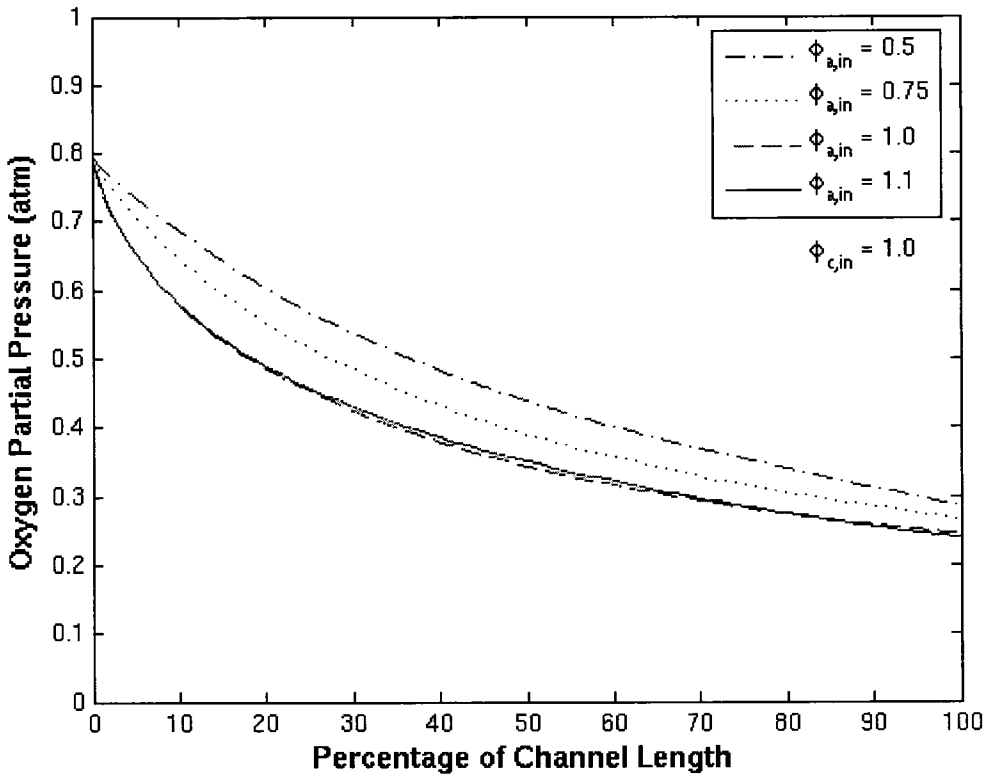


Fig. 22. Effect of anode inlet water content on the partial pressure of oxygen

(Pure oxygen; $\phi_{c,in}$ = 1.0; $\phi_{a,in}$ = 0.5, 0.75, 1.0, 1.1)

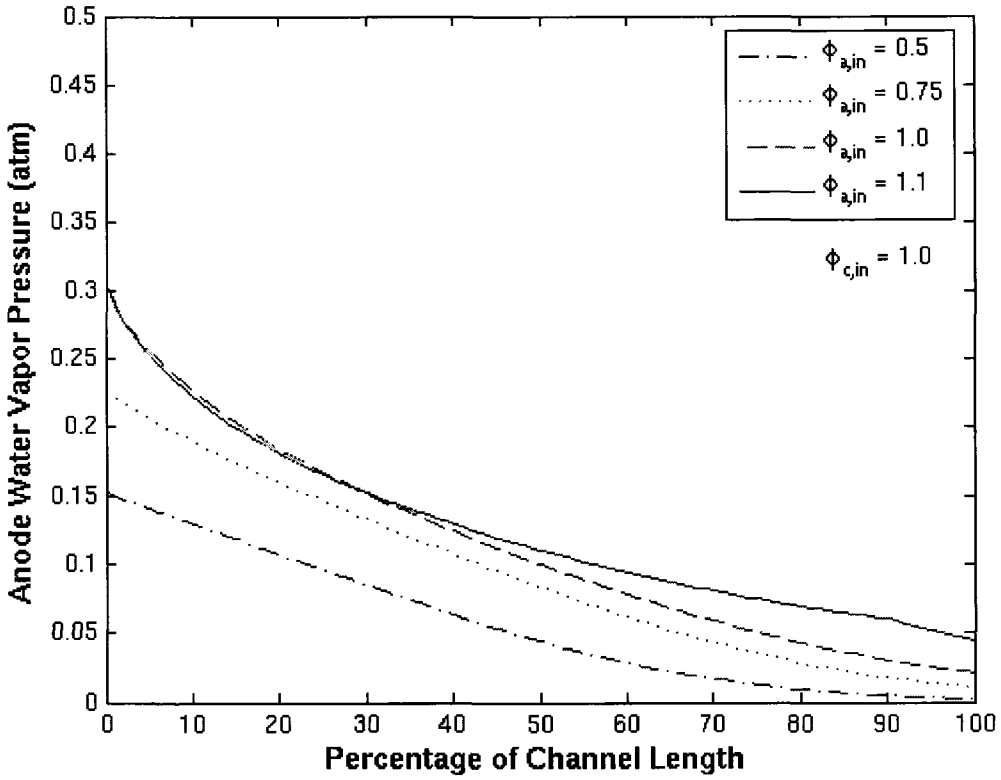


Fig. 23. Effect of anode inlet water content on the water vapor partial pressure on anode side (Pure oxygen; $\phi_{c,in} = 1.0$; $\phi_{a,in} = 0.5, 0.75, 1.0, 1.1$)

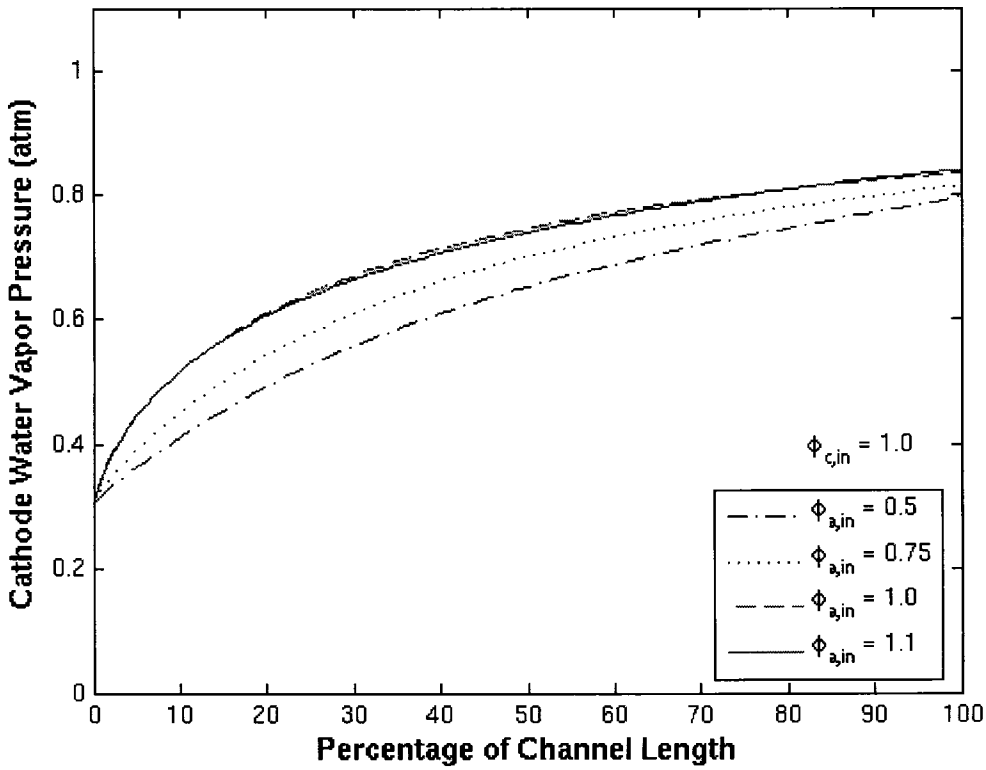


Fig. 24. Effect of anode inlet water content on the water vapor partial pressure on cathode side (Pure oxygen; $\phi_{c,in} = 1.0$; $\phi_{a,in} = 0.5, 0.75, 1.0, 1.1$)

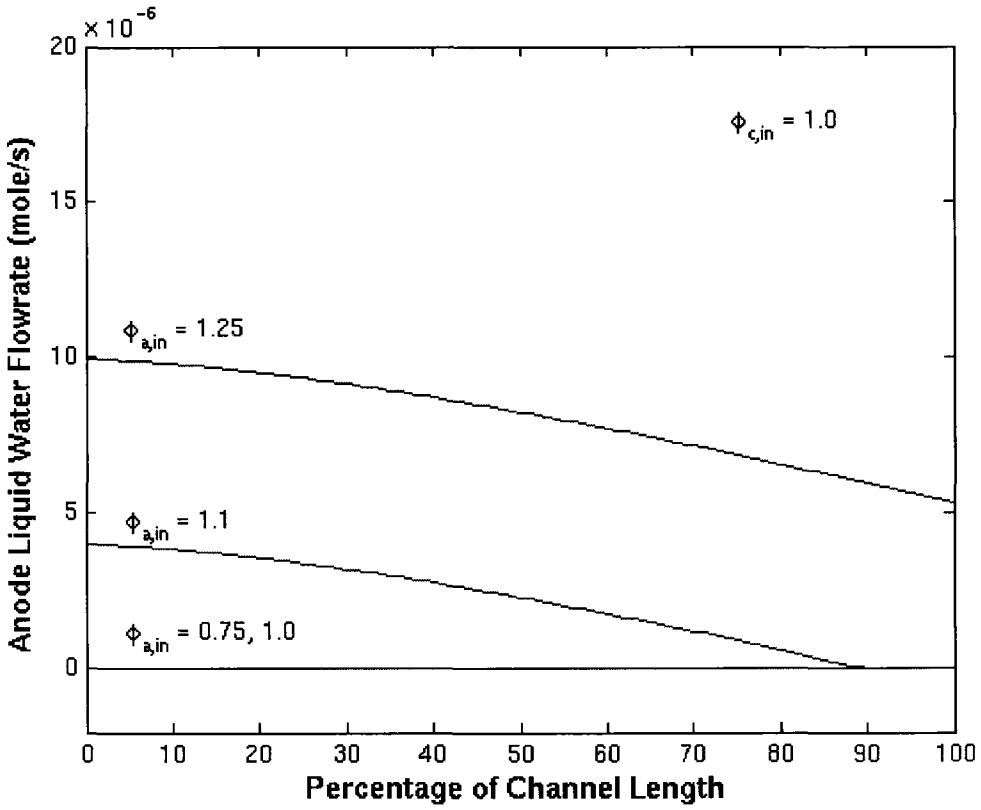


Fig. 25. Effect of anode inlet water content on the liquid water mole number on anode side (Pure oxygen; $\phi_{c,in}$ = 1.0; $\phi_{a,in}$ = 0.75, 1.0, 1.1, 1.25)

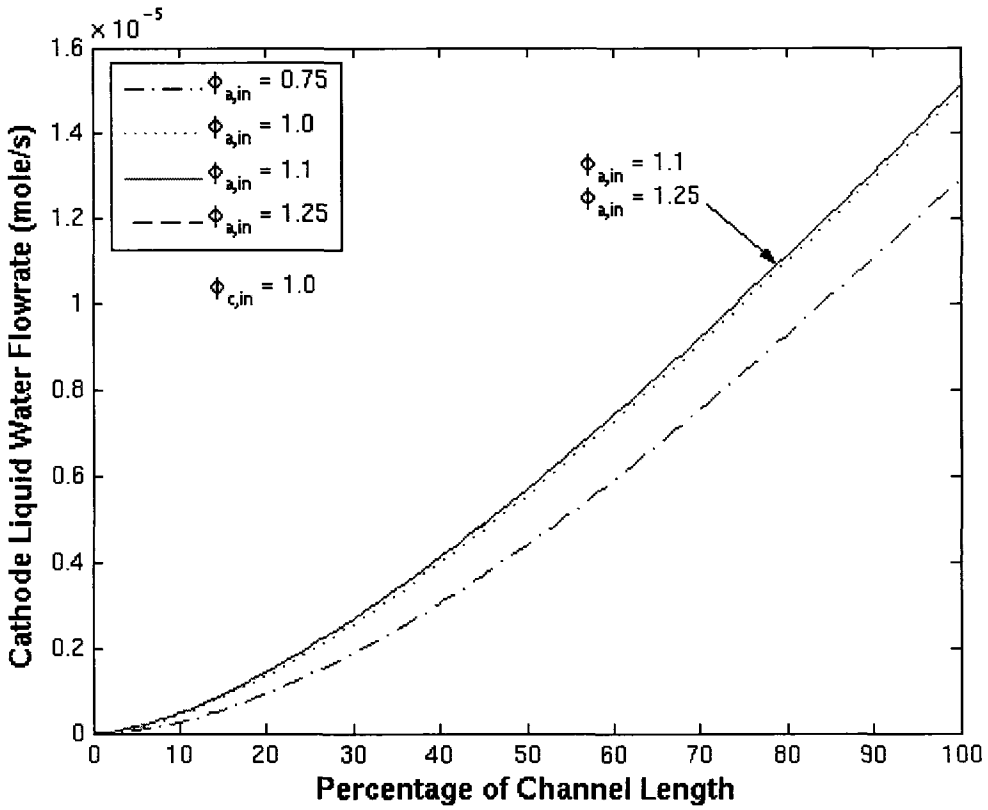


Fig. 26. Effect of anode inlet water content on the liquid water mole number on cathode side (Pure oxygen; $\phi_{c,in}$ = 1.0; $\phi_{a,in}$ = 0.75, 1.0, 1.1, 1.25)

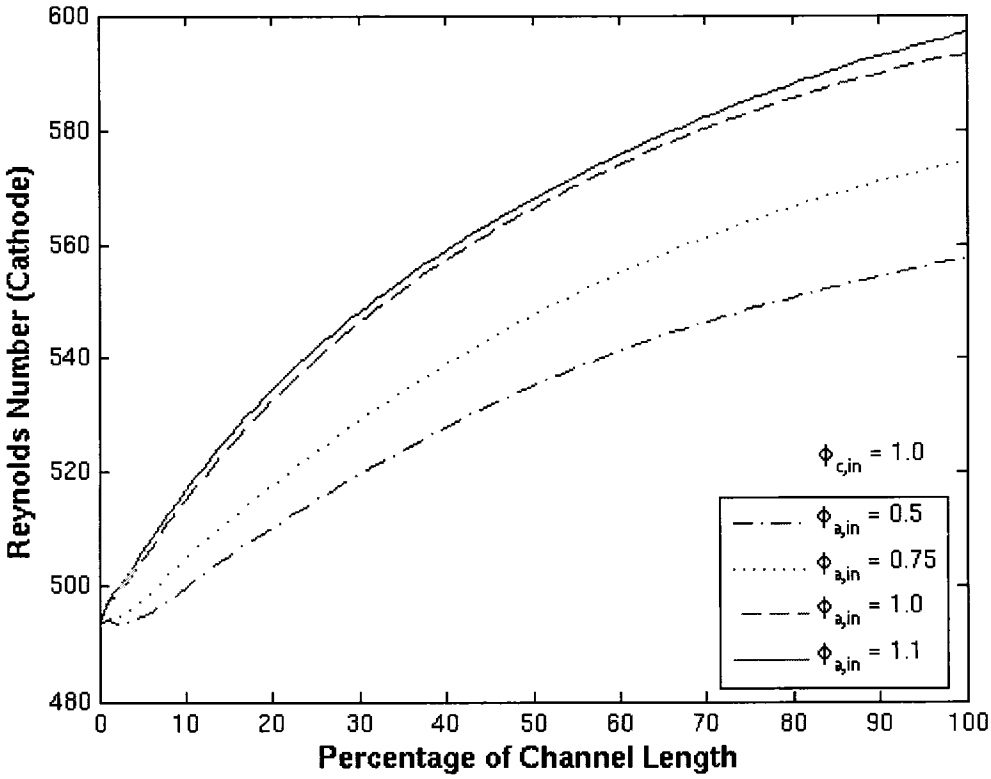


Fig. 27. Effect of anode inlet water content on the Reynolds number in cathode channel (Air; $\phi_{c,in}$ = 1.0; $\phi_{a,in}$ = 0.5, 0.75, 1.0, 1.1)

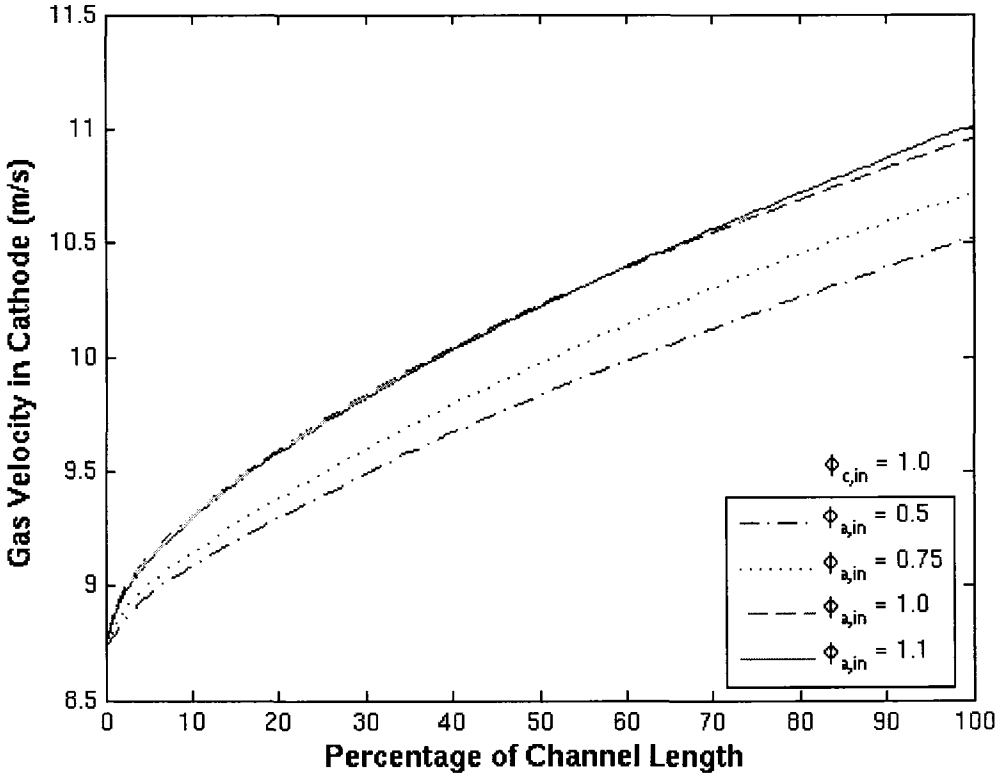


Fig. 28. Effect of anode inlet water content on the gas velocity in cathode channel (Air; $\phi_{c,in}$ = 1.0; $\phi_{a,in}$ = 0.5, 0.75, 1.0, 1.1)

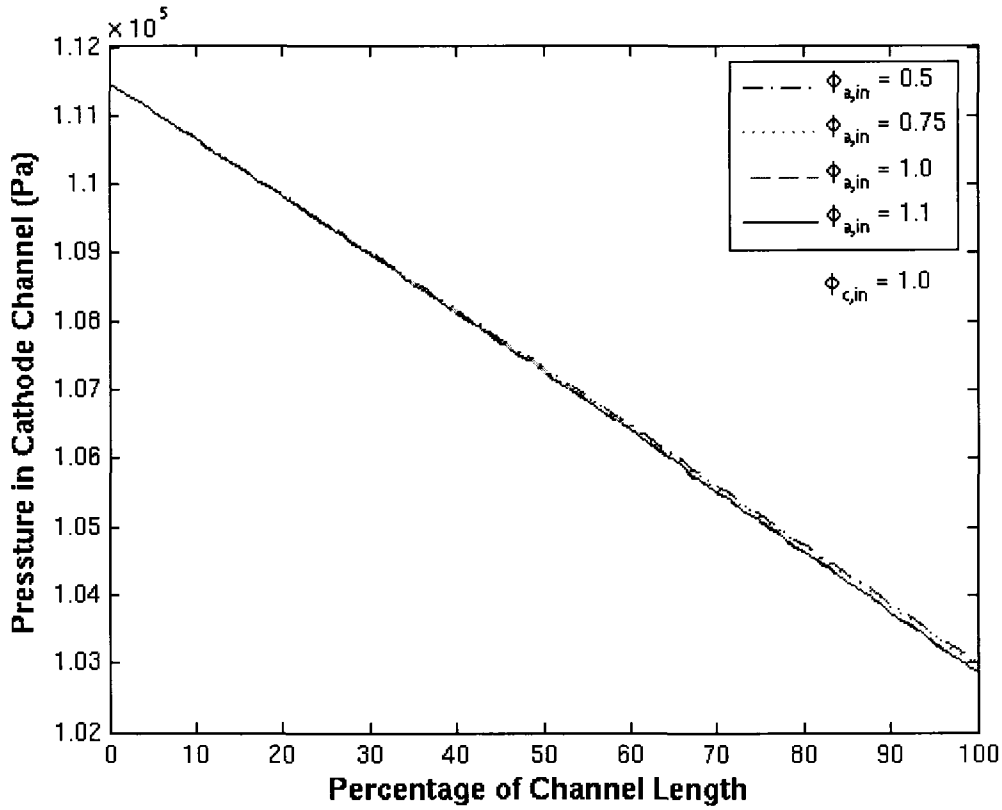


Fig. 29. Effect of anode inlet water content on the local pressure at cathode (Air; $\phi_{c,in} = 1.0$; $\phi_{a,in} = 0.5, 0.75, 1.0, 1.1$)

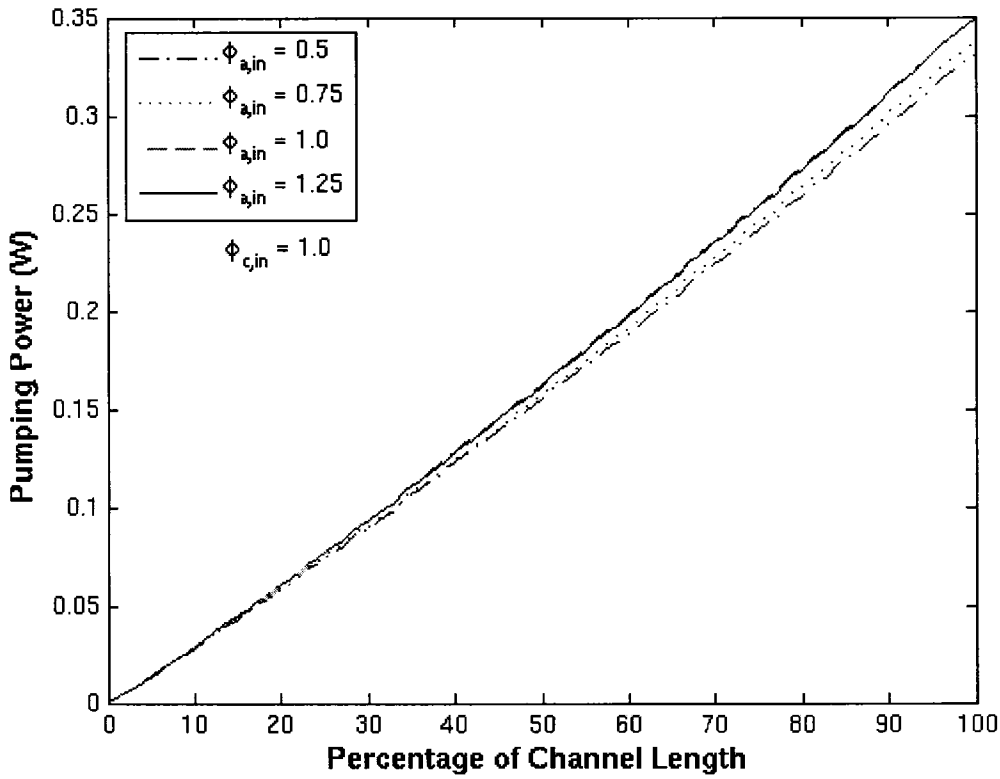


Fig. 30. Effect of anode inlet water content on the required pumping power at cathode (Air; $\phi_{c,in}$ = 1.0; $\phi_{a,in}$ = 0.5, 0.75, 1.0, 1.1)

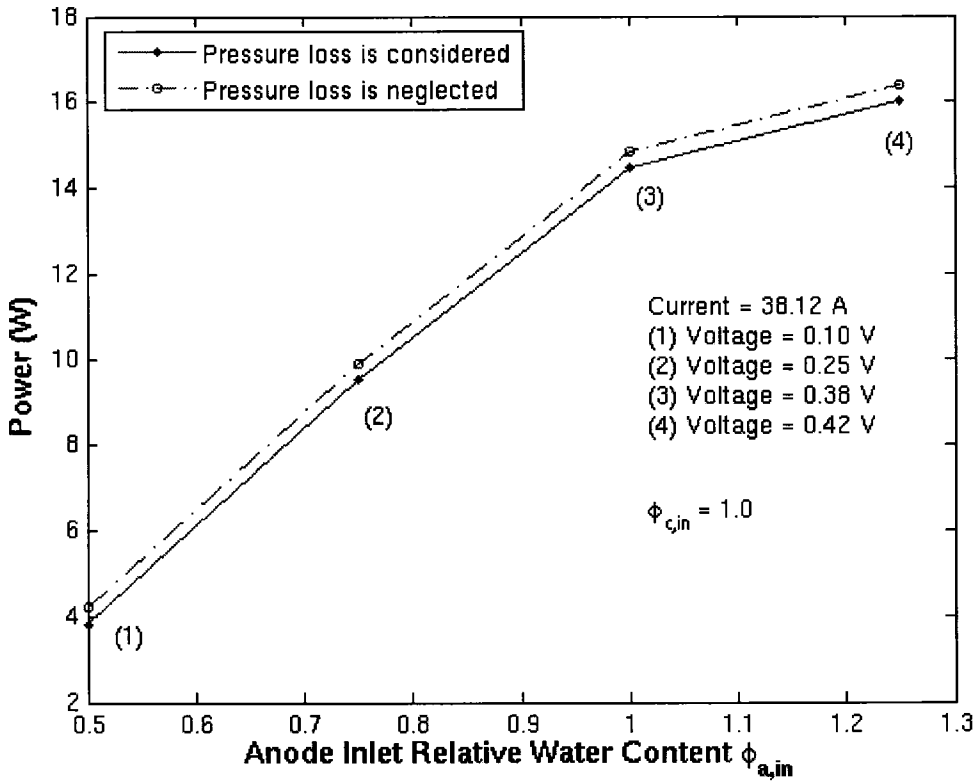


Fig. 31. Effects of anode inlet water content and pressure loss on the power of a single fuel cell (Air)

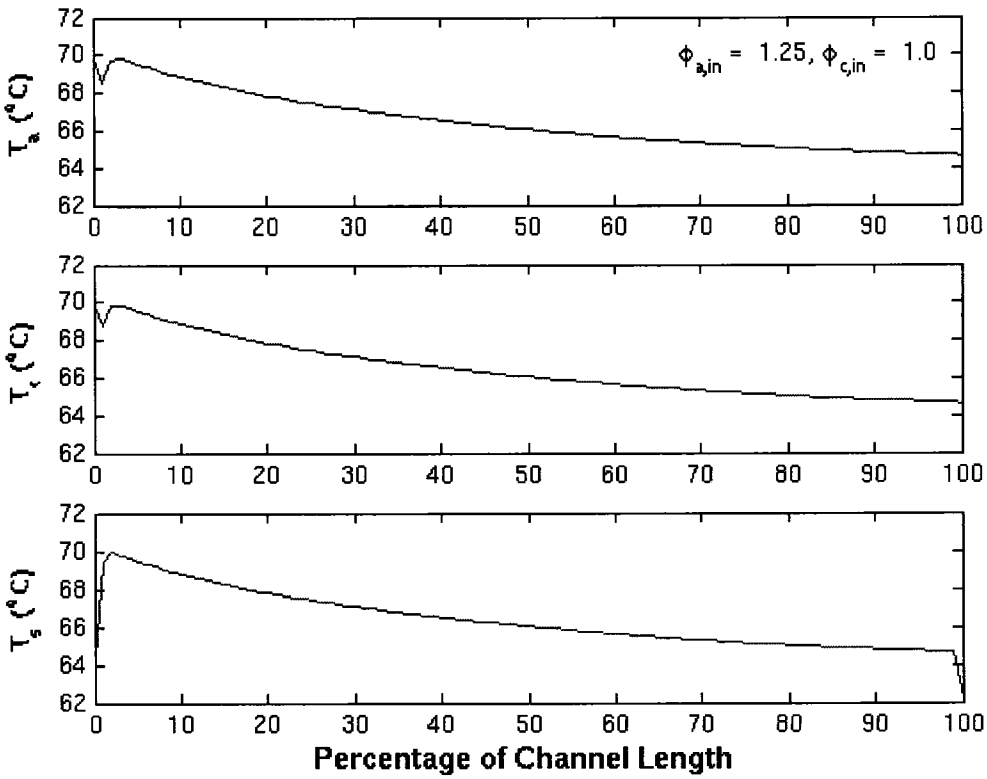


Fig. 32. Temperature profiles along the channels

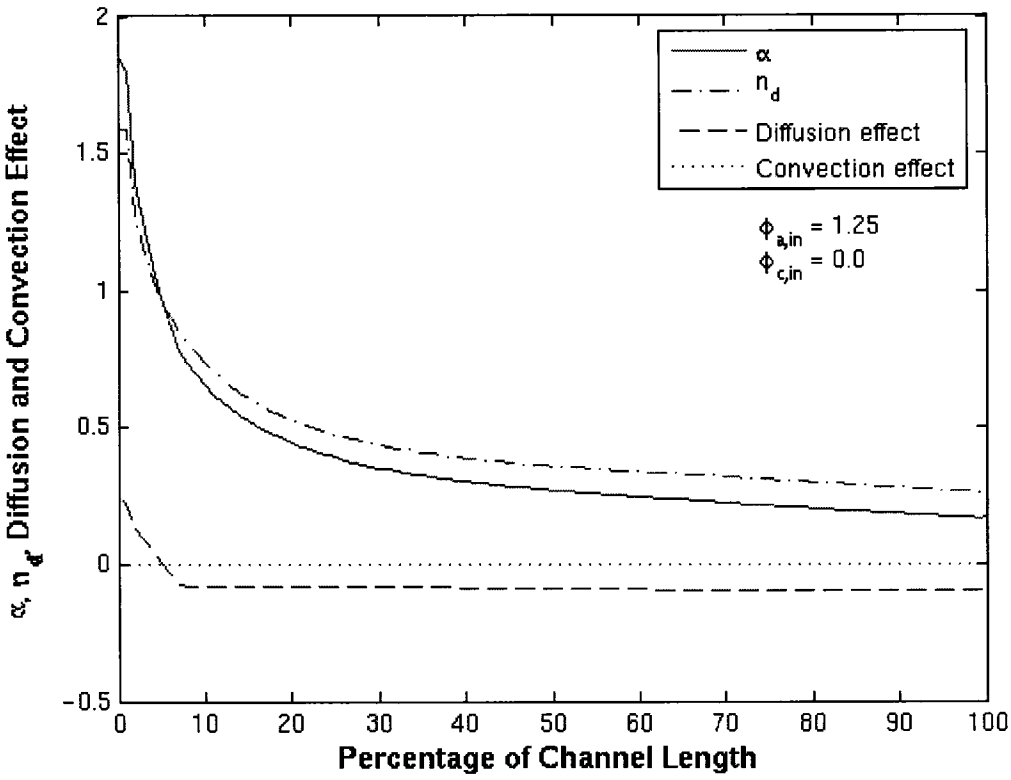


Fig. 33. Contribution of electro-osmotic drag coefficient ($n_d$), diffusion and convection effect on net water flux per proton ($\alpha$)

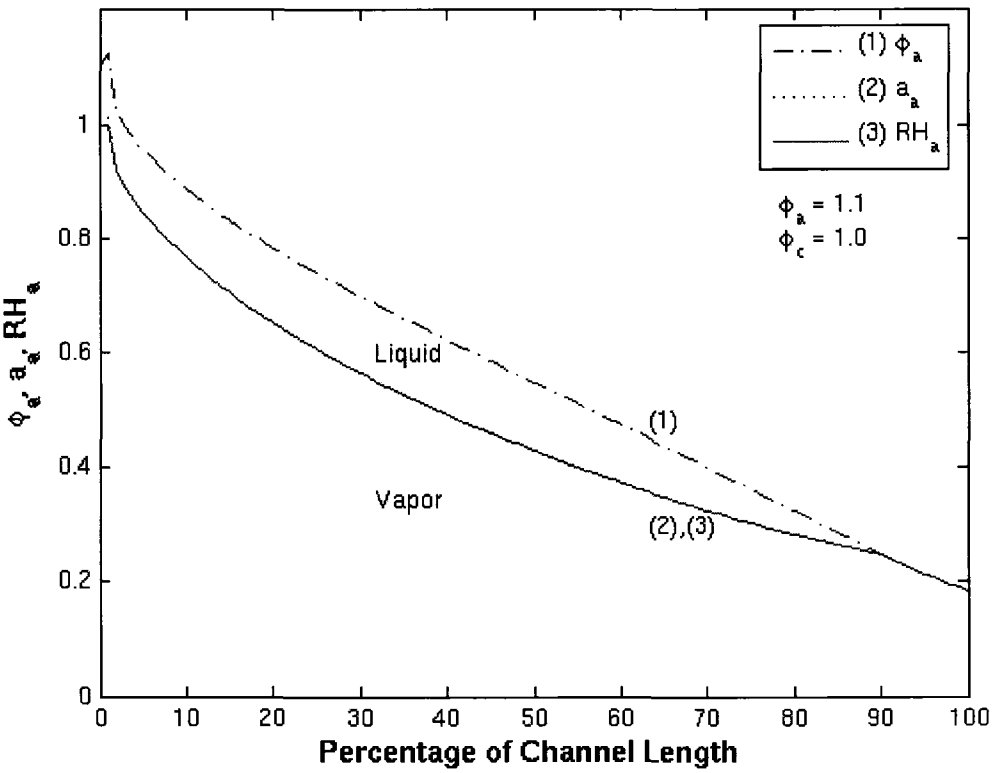


Fig. 34. Water vapor and liquid distribution along the anode flow channel

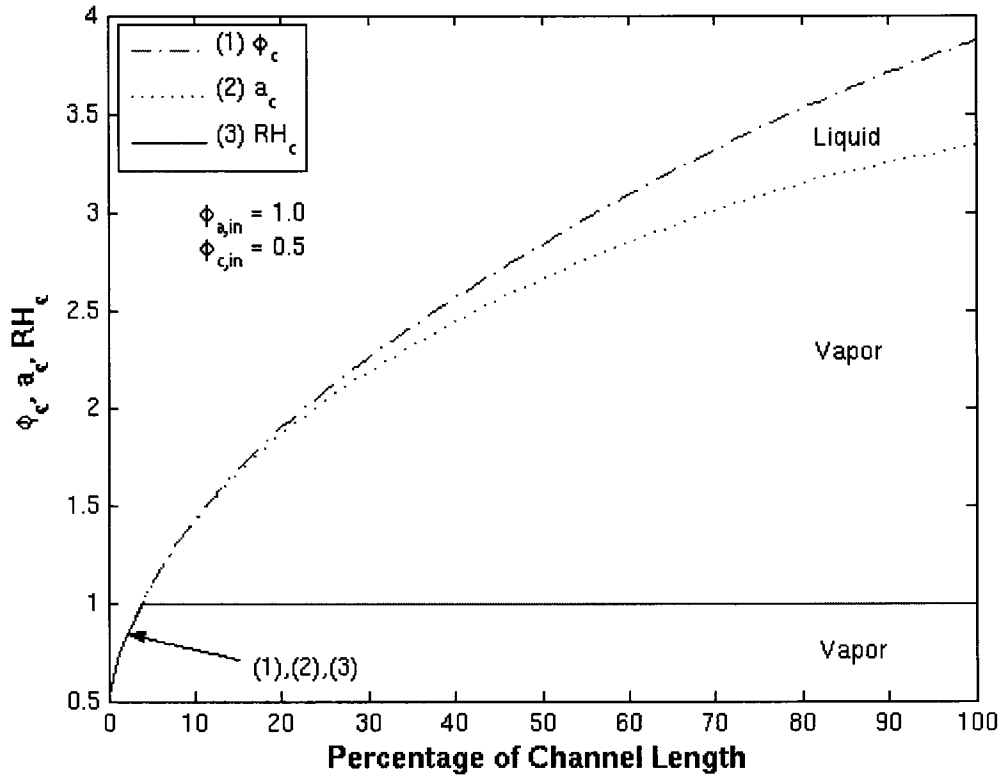


Fig. 35. Water vapor and liquid distribution along the cathode flow channel

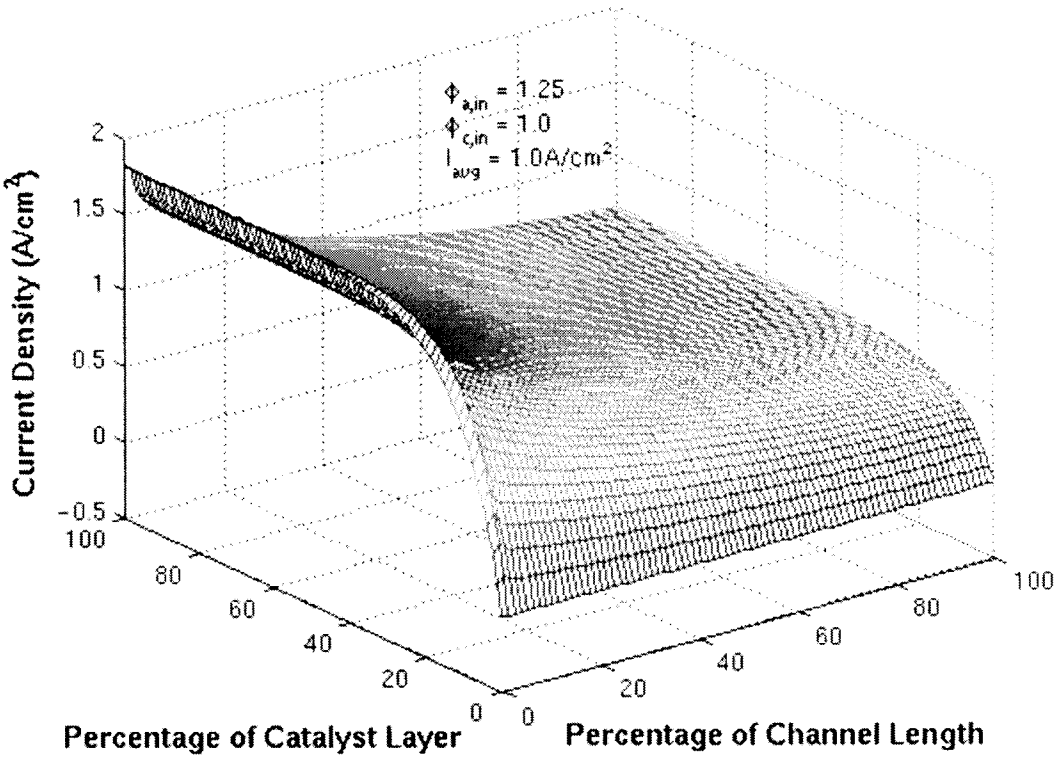


Fig. 36. The distribution of current density within the catalyst layer

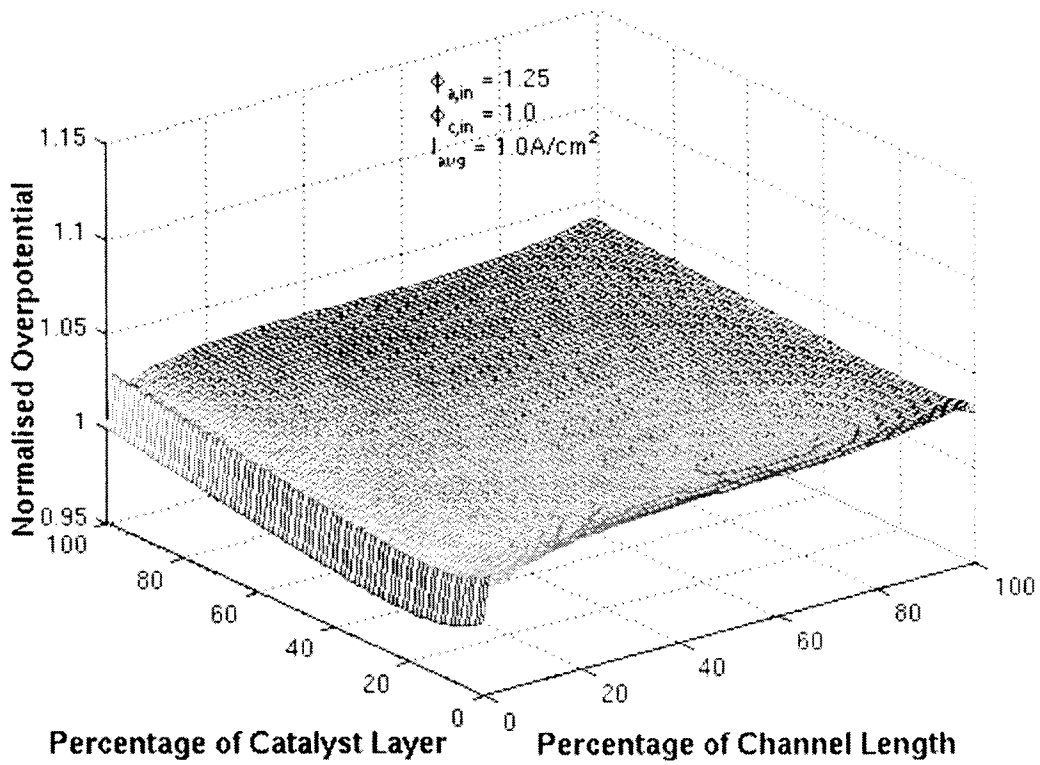


Fig. 37. The distribution of overpotential within the catalyst layer

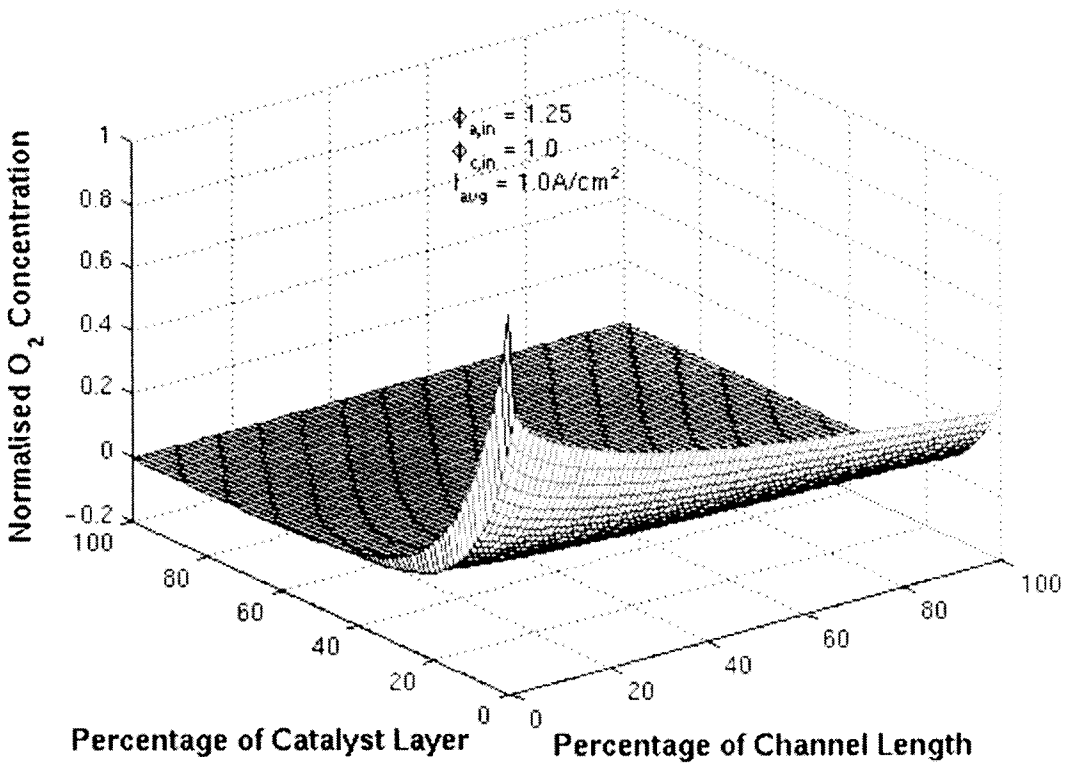


Fig. 38. The distribution of oxygen concentration within the catalyst layer

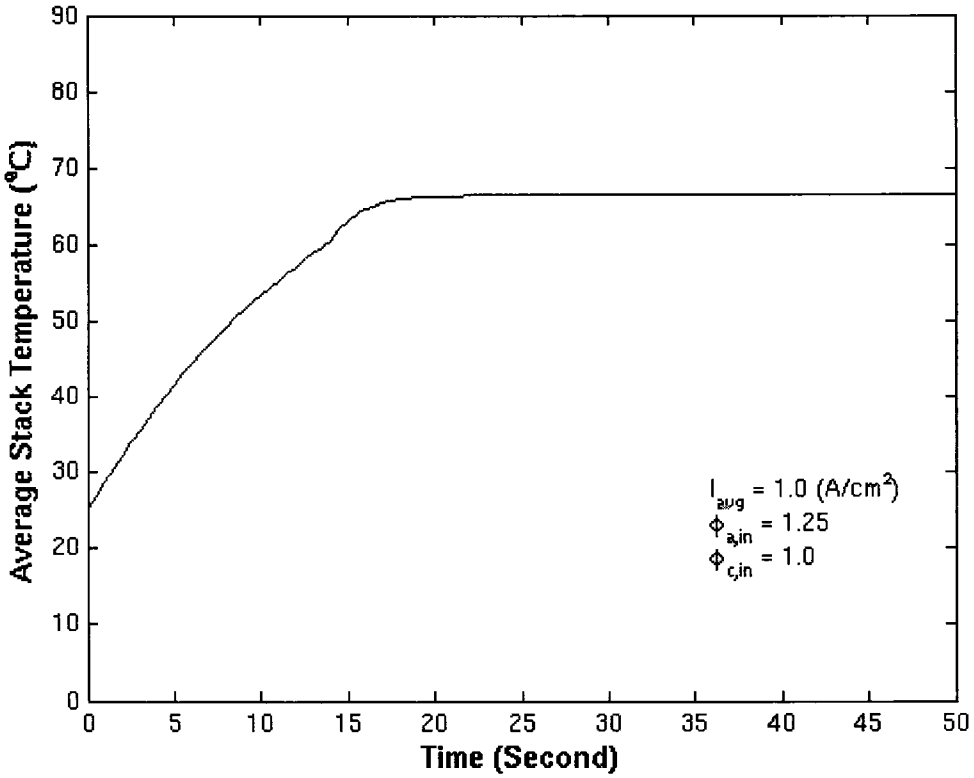


Fig. 39. The evolution of average stack temperature with time using implicit Crank – Nicholson for different time steps

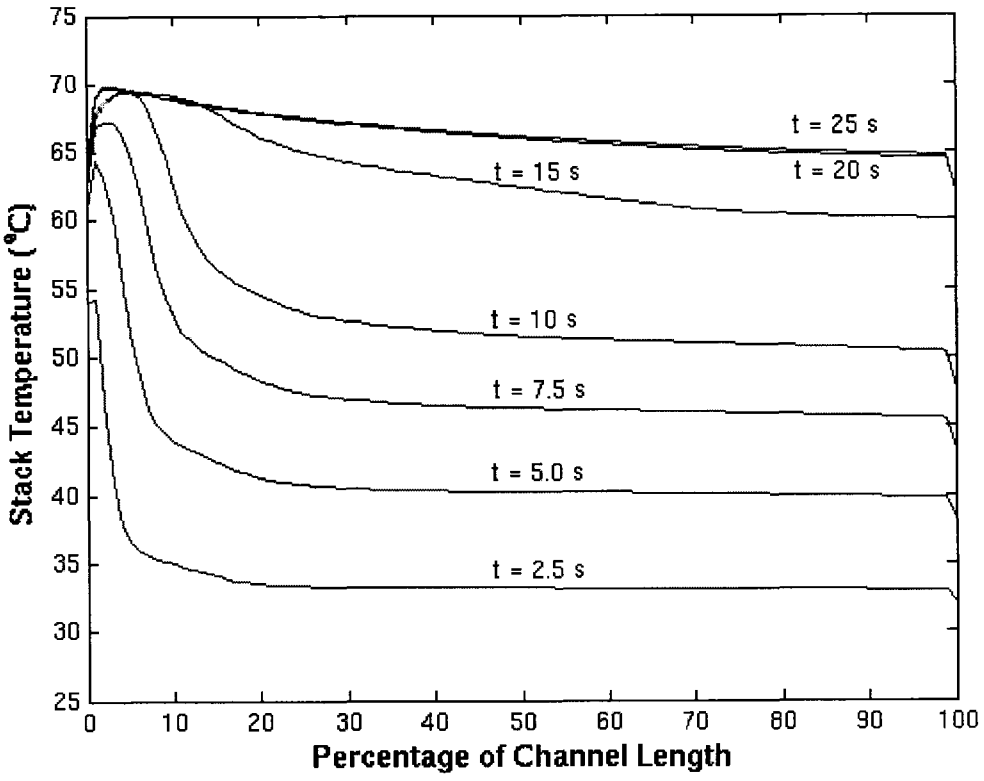


Fig. 40. The evolution of stack temperature profiles with time using implicit Crank – Nicholson for different time steps

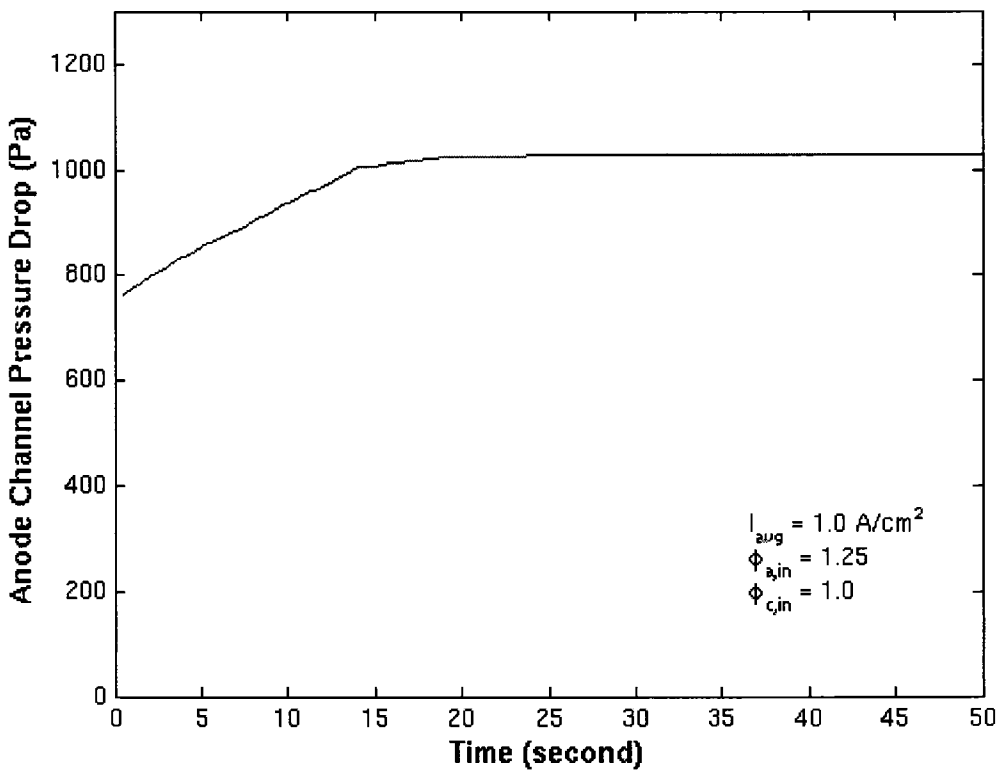


Fig. 41. The evolution of pressure drop in anode channel with time using implicit Crank – Nicholson for different time steps

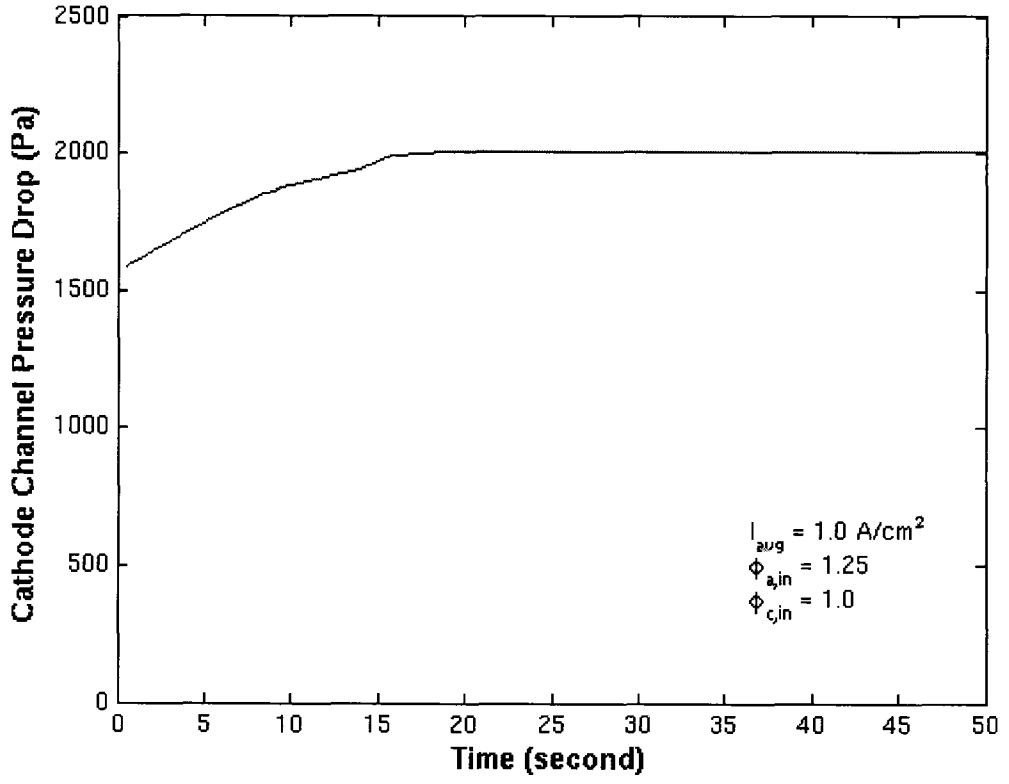


Fig. 42. The evolution of pressure drop in cathode channel with time using implicit Crank – Nicholson for different time steps

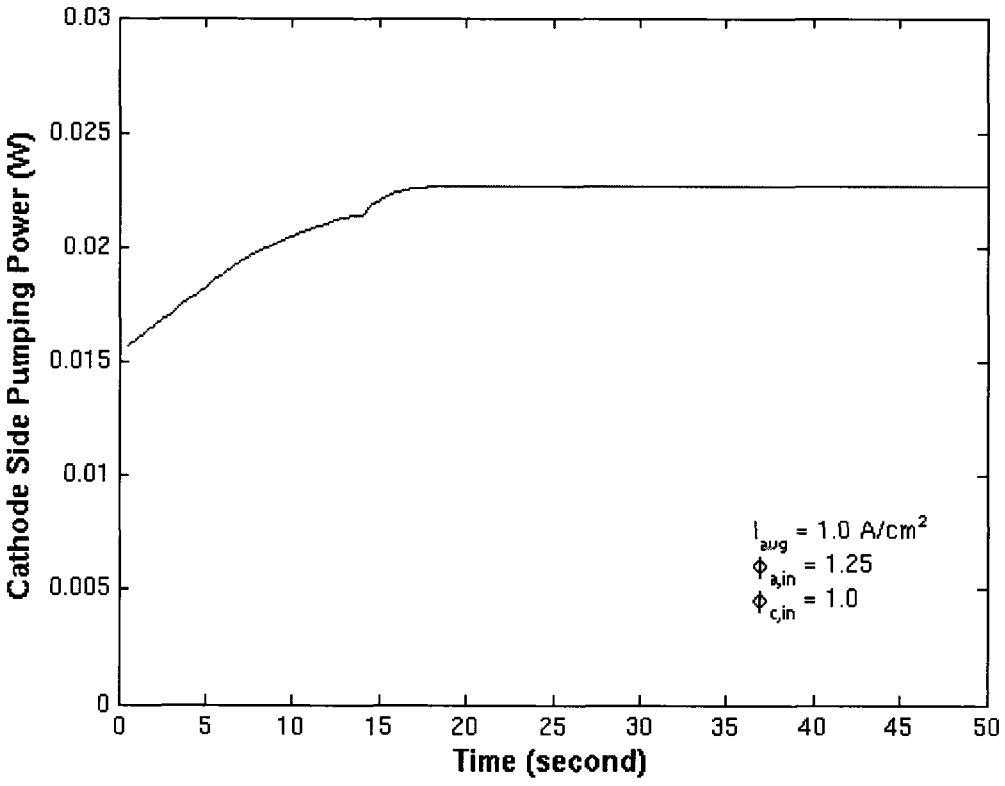


Fig. 43. The evolution of pumping power at cathode side with time using implicit Crank – Nicholson for different time steps

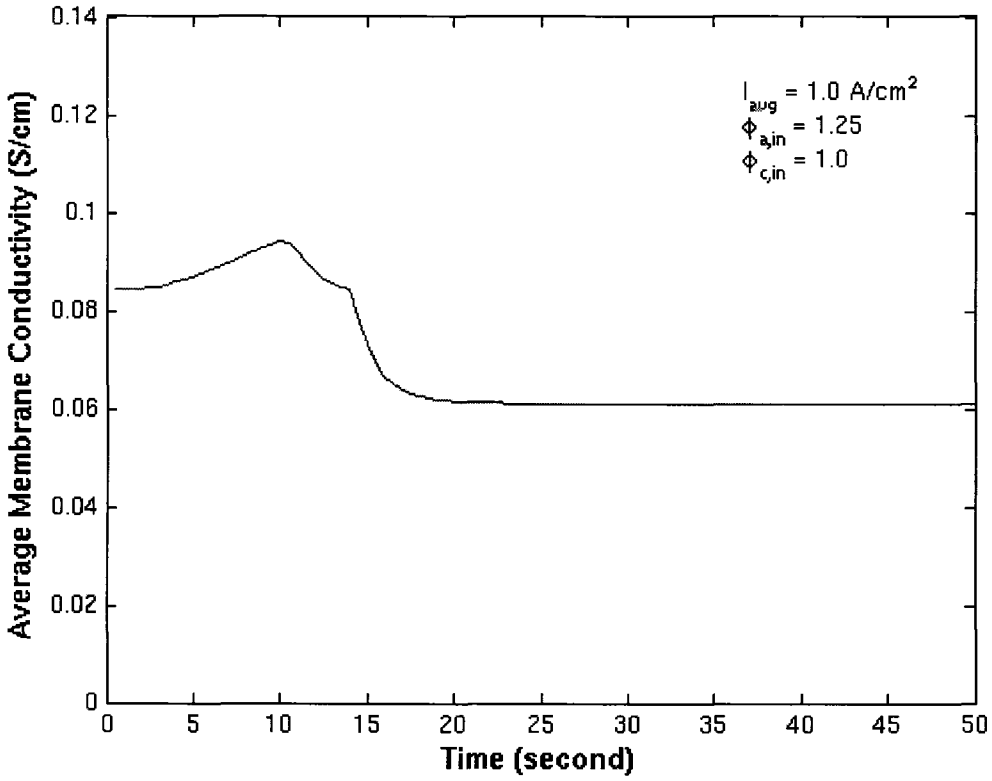


Fig. 44. The evolution of average membrane conductivity with time using implicit Crank – Nicholson for different time steps

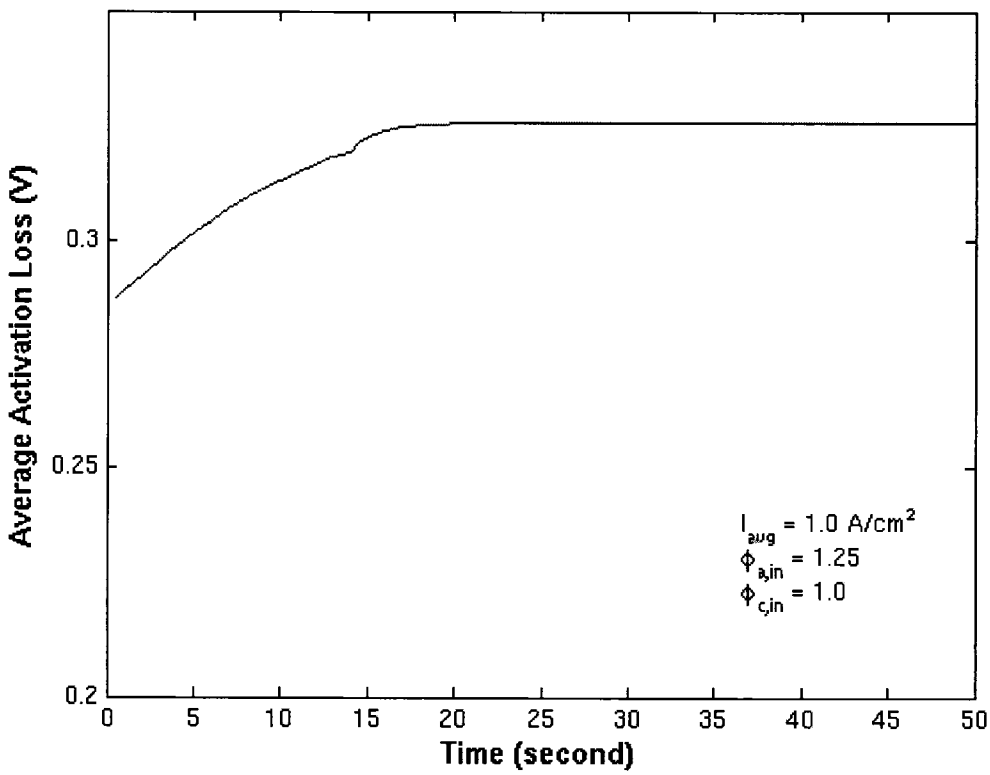


Fig. 45. The evolution of average activation loss with time using implicit Crank – Nicholson for different time steps

Table 1. Representative catalyst surface areas for different catalyst types

| Catalyst type | Surface area / Pt mass $A_s$ ($m^2/g$) |
|---|---|
| 10% Pt on carbon black | 140 |
| 20% Pt on carbon black | 112 |
| 30% Pt on carbon black | 88 |
| 40% Pt on carbon black | 72 |
| 60% Pt on carbon black | 32 |
| 80% Pt on carbon black | 11 |
| Pt black | 28 |

Table 2. Typical dimensions and parameters used in the simulation

| **Parameter** | **Value** |
|---|---|
| Channel length | 95.34 mm |
| Channel width | 0.1 mm |
| Channel height | 0.1 mm |
| Inlet pressure at anode | 1.1 atm |
| Inlet pressure at cathode | 1.1 atm |
| Inlet temperature of flow at anode | 343 K |
| Inlet temperature of flow at cathode | 343 K |
| Anode excess coefficient | 2.0 |
| Cathode excess coefficient | 2.0 |
| Average Current Density | 1.0 A $cm^{-2}$ |
| Permeability of water | $1.58\times10^{-14}$ $cm^2$ |
| Water viscosity | $3.656\times10^{-3}$ g $cm^{-1}$ $s^{-1}$ |
| Heat transfer coefficient | 0.0025 J $s^{-1}cm^{-2}$ $^oC^{-1}$ |
| Dry membrane density | 2.0 g $cm^{-3}$ |
| Dry membrane equivalent weight | 1100 g $mol^{-1}$ |
| Membrane thickness | 0.1275 mm |
| Intradiffusion coefficient of water in membrane | $5.5\times10^{-7}$ $cm^2$ $s^{-1}$ |

Table 3. The effects of pressure loss and anode inlet water content on the power of the single cell

| $\phi_{a,in}$ | 0.5 | 0.75 | 1.0 | 1.25 |
|---|---|---|---|---|
| Voltage (V) | 0.10 | 0.25 | 0.38 | 0.42 |
| Current (A) | 38.12 | 38.12 | 38.12 | 38.12 |
| Power (W) | 3.812 | 9.53 | 14.486 | 16.01 |
| Power loss due to pressure drop (W) | 0.3812 | 0.3812 | 0.3812 | 0.3812 |
| Percentage of power loss | 10 | 4 | 2.6 | 2.4 |

## VITA AUCTORIS

NAME: WENBO HUANG

PLACE OF BIRTH: Shenyang, P.R.China

YEAR OF BIRTH: 1969

EDUCATION:

Master of Applied Science in Mechanical Engineering 2004-2005

University of Windsor, Windsor, ON, Canada

Bachelor Degree in Computer Science 2001-2003

York University, Toronto, ON, Canada

Master of Applied Science in Mechanical Engineering 1991-1994

Northeastern University, Shenyang, China

Bachelor Degree in Mechanical Engineering 1987-1991

Northeastern University, Shenyang, China